Designing IR Imaging Devices Using An Inkjet Printing System

Younsu Kim

A thesis

submitted in partial fulfillment of the

requirements for the degree of

Master of Science

University of Washington

2018

Committee:

Wei-Chih Wang, Chair

Mark Tuttle

Albert Kobayashi

Program Authorized to Offer Degree:

Mechanical Engineering

University of Washington

Abstract

Designing IR Imaging Devices Using an Inkjet Printing System

Younsu Kim

Chair of the Supervisory Committee:
Wei-Chih Wang
Mechanical Engineering

Thermal imaging devices and sensors are used in a variety of different fields, such as in cybersecurity. These devices are commonly made with semiconductors and pyroelectric materials. In some field and applications, a device may be needed in order to detect electromagnetic radiation. One method that has yet to be looked at extensively for creating imaging devices is inkjet printing. Inkjet printing involves the use of a nozzle or jet head to deposit ink onto a substrate in order to build a structure. In this study, an inkjet printing system was tested and used to fabricate a resistive thermal imaging device that is much smaller and simpler in design than traditional imaging devices. The imaging device was created using a conductive polymer rather than traditional manufacturing materials for thermal imaging devices. The sensitivity of the imaging device was analyzed under different environments in order to see how the performance of the device can be optimized.

This page is intentionally left blank.

TABLE OF CONTENTS

List of Figures iii

List of Tables vi

Chapter 1. Introduction 1

1.1 Overview 1

1.2 Thesis Objective and Outline 3

Chapter 2. Background and Literature Review 5

2.1 Inkjet Printing 5

2.1.1 Optical Microresonator Sensor 5

2.1.2 Photonic Biosensors 6

2.1.3 Potentiometric Ion-Sensing Devices 7

2.1.4 Plate Wave Acoustic Sensor 8

2.2 Thermal Imaging Devices 9

2.2.1 Superconducting Bolometer For Fourier transform spectroscopy 9

2.2.2 Room Temperature Bolometer 11

2.2.3 Pyroelectric Detectors with NiCr Thin-Film Absorber 12

2.2.4 CMOS Microbolometers 14

2.2.5 High-Responsivity Thermoelectric Infrared Detector 15

2.3 Thermal Imaging Device Comparison 17

Chapter 3. Inkjet Printing System 19

3.1 Jet Head and Amplifier 19

3.2 Stage and Motion Controller 21
3.3 Data Acquisition System 22
3.4 Inkjet Printing System Set-Up 24
3.5 Software Components 27
3.5.1 Pattern Generation and Processing Module 28
3.5.2 Waveform Generation Module 31
3.5.3 Stage Control Module 33
Chapter 4. Resistive Thermal Imaging Device Design 37
4.1 Printing a Column 37
4.2 Design and Fabrication Of Imaging Device 40
Chapter 5. Device Test Results 47
5.1 Test Set-Up 47
5.2 Resistance vs Substrate Temperature 48
5.3 Resistance Change vs Source Distance Above Room Temperature 50
5.4 Resistance Change vs Source Distance Below Room Temperature 57
5.5 Discussion 60
5.6 3 by 3 Array and Issues 62
Chapter 6. Conclusion And Future Works 64
Bibliography 66

LIST OF FIGURES

Figure 1. Concave FP sensor design [8] 6
Figure 2. Potentiometric device fabrication process [10] 8
Figure 3. Completed sensor [11] 9
Figure 4. Transition edge sensor bolometer prototype. The thermistor is located in the center. The leads of the thermistor go to the left. The gray area represents the metal mesh absorber [12]. 10
Figure 5. Bolometer at the center of the spiral antenna [13] 11
Figure 6. Voltage responsivity of bolometers. For each of the bolometers, the solid line represents the calculated responsivity and the symbols represent the responsivity that was measured [13]. 12
Figure 7. SEM image of a three-layer NiCr absorber structure deposited at varying angles of incidence [14] 13
Figure 8. Spectral responsivity of the pyroelectric detectors [14] 13
Figure 9. SEM micrograph of a serpentine structured microbolometer with additional dielectric bridges [15] 14
Figure 10. Resistance vs temperature plot [15] 15
Figure 11. Thermoelectric IR detector structure [16] 16
Figure 12. Responsivity vs chopping frequency [16] 17
Figure 13. Printing system summary with major components 19
Figure 14. Jet head 20
Figure 15. Power amplifier 20
Figure 16. Linear translation stages 21
Figure 17. Newport Motion Controller ESP 300 22
Figure 18. NI DAQPad – 6259 23
Figure 19. LED strobe 23
Figure 20. Jet head after clamping 24
Figure 21. Reservoir 24

Figure 22. Pressure regulator valves 25
Figure 23. Amplifier connections. The red clip of the amplifier connects to the analogue 0 of DAQPad and the black clip connects to the ground. 26
Figure 24. Microscope camera set-up 26
Figure 25. Inkjet printing system with the devices connected and organized 27
Figure 26. Pattern generation and processing module 29
Figure 27. Pattern generation and processing module LabVIEW block diagram 29
Figure 28. Scaling factor code in LabVIEW 30
Figure 29. Waveform generation LabVIEW code 32
Figure 30. ESP-300 library functions code 34
Figure 31. Checking the tolerance in the X and Y directions 35
Figure 32. DAQ assistant actuating the jet head and the LED strobe 36
Figure 33. Clear jet head 38
Figure 34. Jet head with PEDOT at the tip 38
Figure 35. PEDOT column at the beginning of the print 39
Figure 36. PEDOT column after 200 drops 40
Figure 37. Patterns tested in ANSYS simulations 41
Figure 38. Zig zag print pattern 42
Figure 39. Printed zig zag pattern 43
Figure 40. Contact pads 44
Figure 41. Fully fabricated resistive device 45
Figure 42. 3 by 3 array pattern 46
Figure 43. Printed 3 by 3 array pattern 46
Figure 44. Initial resistance measurement set-up 48
Figure 45. Average resistance vs PDMS temperature with error bars 49
Figure 46. Sensitivity test set-up 51
Figure 47. Average resistance change vs 14.5^{o}C steel rod distance with error bars 53
Figure 48. Average resistance change vs 50.5^{o}C steel rod with error bars 55
Figure 49. Average resistance change vs finger distance with error bars 57
Figure 50. Measurement set-up with freeze pack underneath 57

Figure 51. Top view of the measurement set-up with freeze pack underneath 58
Figure 52. Average resistance change vs source distance with PDMS around freezing temperatures 60
Figure 53. Thermal image from 3 by 3 array – obtained from ANSYS simulation 62
Figure 54. 3 by 3 array sample simulation 63
Figure 55. Array circuits. The resistors in the circuits represent pixels, and the circled numbers represent contact pads. 65

LIST OF TABLES

Table 1. Thermal imaging device comparison chart 18
Table 2. Clevios PH 1000 properties 37
Table 3. Results from each tested geometry 41
Table 4. Resistance measurements at different PDMS temperatures 49
Table 5. Sensitivity test results with 14.5ºC steel rod above the sensing area 52
Table 6. Sensitivity test results with 50.5ºC steel rod above the sensing area 54
Table 7. Sensitivity test results with finger above the sensing area 56
Table 8. Resistance measurements with PDMS around freezing temperature 58
Table 9. Sensitivity test results with PDMS around freezing temperature 59

ACKNOWLEDGEMENTS

I would like to first thank Prof. Wei-Chih Wang, my research advisor and thesis committee chair, for the support and confidence that he showed in me throughout this project. He guided me through all of the ups and downs and helped me grow as a researcher and engineer. He has also provided me with advice as I graduate and enter the real world. I would also like to thank Ben Estroff and Chun-Wei Wu for all of the assistance that they provided me with during the fabrication process. They taught me the different parts of the inkjet printing system. I would like to thank Abhishek Gupta for assisting me with the simulations. I would also like to thank Prof. Albert Kobayashi and Prof. Mark Tuttle for being a part of my thesis committee and providing excellent feedback regarding this research. I am also grateful to Chi Leung Tsui, David Schipf, and other members of the UW Microtechnology Lab for all of the research advice that they have given me. I will always be thankful for the way in which the UW Mechanical Engineering Department accepted and supported me. Finally, I would like to thank my parents and my sister for all of the financial and emotional support that they showed me. They have helped me accomplish so much during my time at UW. Without them, I would not be the person that I am today.

Chapter 1. INTRODUCTION

1.1 OVERVIEW

Additive manufacturing is a process in which objects are built by piling layers of material on top of each other. Over the years, additive manufacturing has grown in popularity due to advantages such as cost and speed. There are many different types of additive manufacturing processes, such as powder bed fusion and directed energy deposition. In powder bed fusion, a laser or another energy source is used to scan and melt a layer of powder into a desired shape [1]. Directed energy deposition is a process in which materials are melted and fused together as they are deposited. A thermal energy source is used to fuse the materials [1]. Other examples of additive manufacturing processes include vat photopolymerization, material extrusion, and sheet lamination. 3D printers are commonly used in additive manufacturing processes.

For small scale prints, inkjet printing is an extremely promising additive manufacturing process. Inkjet printing is a process in which a liquid ink is ejected through a micrometric nozzle onto a substrate or surface in order to create patterned layers [2]. For the most part, inkjet printing is a method that can be used to design flexible electronics. Inkjet printing has a number of advantages over other processes. For instance, inkjet printing can be a much more accurate design process compared to other methods. This advantage in accuracy may be due to the jet head that is used in an inkjet printer. The size of a jet head is extremely small, so as a result, the jet head spits out small droplets that can be seen with a microscope. Inkjet printing can also be cheaper compared to other additive manufacturing processes. On the other hand, the size and features of an inkjet printer can also lead to some disadvantages, such as the amount of time that it takes to print. Inkjet

printing is a method that may take a little more time compared to other printing methods because more passes may be needed in order for an inkjet printer to print or deposit an item. Nevertheless, this is a process that has been used to successfully create a variety of different sensors and/or devices.

In particular, thermal imaging devices are highly used in a variety of fields today, such as in the medical field. Imaging devices are commonly used in the medical sector in order to detect radiation leaks or inflammation within a human body [3]. This allows doctors to diagnose diseases. One type of thermal imaging device that is fairly common in the world is a bolometer. A bolometer is a thermal infrared sensor that can absorb electromagnetic radiation and produce a temperature change [4]. The temperature change then results in an electrical resistance change in a defined sensing element [5]. The resistance change can be turned into a thermal image. Ideally, bolometers should be built with materials that have a high temperature coefficient of resistance so that they are more sensitive [5]. Thermoelectric IR detectors and pyroelectric sensors are two other examples of commonly used thermal imaging devices. A thermoelectric IR detector is a device that detects radiation in a way that is similar to that of a bolometer. A thermoelectric material is used to sense temperature differences between the detector's absorber and the surrounding environment. A voltage is produced in the material when there is a temperature difference [16]. In pyroelectric sensors, a pyroelectric material is used to produce a variation in induced charge and a pyroelectric current when the material changes temperature from infrared radiation [6]. In general, these three types of thermal imaging devices are capable of excellent, consistent performance. In spite of that, each of these devices have some drawbacks. In order to create bolometers, a clean room and high precision 3D fabrication process is often needed. This fabrication process can take some time. Thermoelectric IR detectors and pyroelectric sensors may have a short working or

detection distance. As a whole, thermal imaging devices have been designed using a variety of different methods and materials. However, inkjet printing does not appear to be a method that has been commonly used when it comes to designing thermal imaging devices. In addition, thermal imaging devices seem to be frequently made with semiconducting and/or pyroelectric materials rather than polymers [7]. Therefore, it would be highly interesting to see whether the inkjet printing method and conductive polymers can be used to successfully design a resistive thermal imaging device that addresses the shortcomings of traditional imaging devices.

1.2 Thesis Objective and Outline

The goal of this research is to design polymer-based, resistive thermal imaging devices through inkjet printing and determine whether inkjet printing is a feasible process for imaging device design. Poly(3,4-ethylenedioxythiophene) polystyrene sulfonate (PEDOT:PSS), which is a conductive polymer, will be mainly used to create the devices. After the devices are designed, they will be evaluated based on their sensitivity. The sensitivity of the devices can be evaluated by applying a heat source, such as a human finger, near the sensing element of the device and measuring the corresponding electrical resistance change. If resistive thermal imaging devices can be successfully created, then it may also be possible to implement these devices into soft wearable sensors that can be used in different ways. For instance, wearable sensors may be utilized as part of military equipment in order to detect a human body through a wall. Wearable sensors can also be implemented in commercial applications in order to figure out where a pipe leakage has occurred. All in all, wearable sensors have a wide range of potential applications.

This thesis will cover all aspects of the research. Previous studies on inkjet printing and thermal imaging devices will be in Chapter 2. In Chapter 3, the inkjet printing system that was

used in this research will be discussed. Chapters 4 and 5 will cover the imaging device fabrication process and the results that were obtained from testing the device. Chapter 6 will describe the main takeaways from this research and how this research can be used going forward.

Chapter 2. BACKGROUND AND LITERATURE REVIEW

2.1 INKJET PRINTING

We looked at a number of previous studies that focused on the use of inkjet printing to fabricate sensors and devices. These studies are summarized in this section.

2.1.1 *Optical Microresonator Sensor*

There has been a study on the use of inkjet printing in order to create an optical microresonator sensor. This study was based on photoacoustic imaging and the creation of a Fabry Perot (FP) ultrasound sensor, which can be used in a number of photoacoustic imaging applications [8]. One of the concerns with the sensor is the limited sensitivity that can occur when the laser beam that is focused on the etalon/sensor diverges in a direction. Therefore, this study looked into a sensor design that may resolve this problem. The original sensor that was looked at was a planar FP sensor. The planar FP sensor was made using a number of materials, such as a polymer spacer, which was placed between two dichroic mirrors [8]. There was also a polymethylmethacrylate (PMMA) backing stub that is transparent. The study looked at the phase interferometer transfer function as well in order to see changes in the reflected optical power. The study also looked into a concave FP sensor that can potentially improve the optical sensitivity of the sensor.

Inkjet printing was used to create a number of parts that made up the concave sensor. Figure 1 on the next page shows the design of a concave FP sensor. One part that was printed was a UV curable optical adhesive dome. Inkjet printing was used because inkjet printing can produce extremely high accuracy in terms of volume. The concave sensor was then tested. The study looked at the sensor's ITF, noise-equivalent pressure, and its frequency response [8]. The results showed

that the sensitivity of an acoustic sensor can be increased significantly if the sensor uses a concave shape rather than a standard planar sensor.

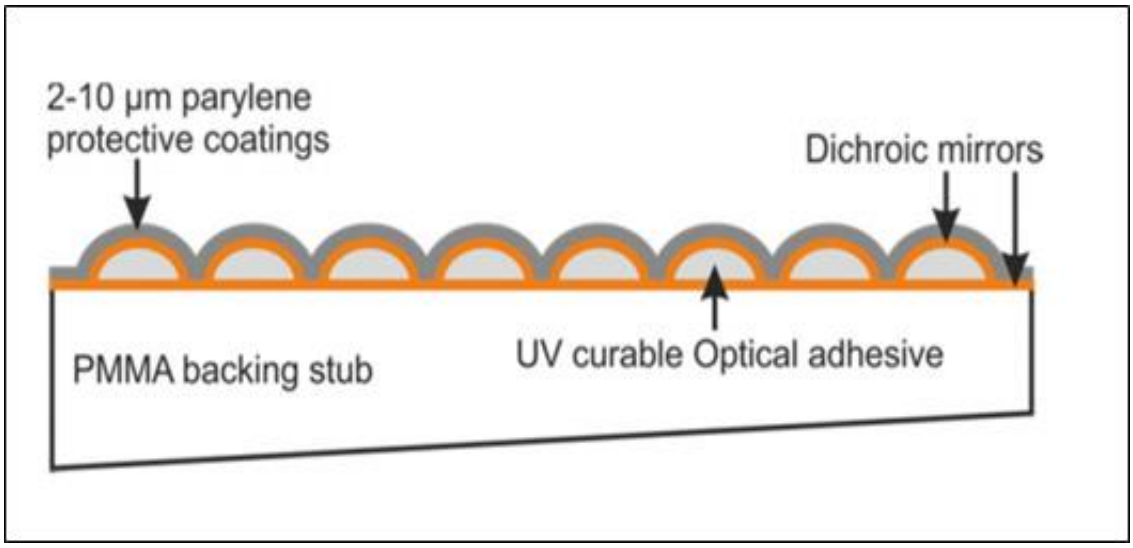

Figure 1. Concave FP sensor design [8]

2.1.2 *Photonic Biosensors*

A previous study focused on the design of optical waveguide based biosensors. For these sensors, inkjet printing is considered to be a potential method of design because inkjet printing may be more suited for the deposition of certain solutions that are needed [9]. The sensor chips that were looked at in the study appear to be from manufactured silicon nitride waveguides. One of the steps that the study looked at during its design process was surface modification. Specifically, the study looked at polyethylenimine (PEI-B) and the benzo-dextran to functionalize biosensors. Before the inkjet printer was used, there were some solutions that were prepared for different polymers. Afterwards, the inkjet printing process was used in order to create a number of surface modifications. The surface modifications that were printed were a PEI-B surface, hydrogel thin film on top of a PEI-B surface, a hydrogel thin film containing PEI-B on a normal surface,

and a plain hydrogel thin film on a normal surface [9]. Besides the surface modifications, this study looked at the possibility of binding C-reactive protein (CRP). For this part, the study focused mainly on a monoclonal antibody and a DNA-aptamer. Additionally, the study looked into the hydrogel film thickness, as well as the hydrogel thin films' interactions with CRP and antibodies and whether the films can be used to detect CRP. The results of the study showed that inkjet printing may have the ability to improve the interferometric, optical waveguide based sensors, and that the use of PEI-B with hydrogel thin films is something that should be considered when designing these sensors.

2.1.3 *Potentiometric Ion-Sensing Devices*

There is a previous study done on the design of disposable ion-sensing devices. The design process in this study involved the creation of electrodes using inkjet printing. Filter papers were also used in the design. The design process involved the use of PEDOT:PSS ink for printing. In order to prepare the PEDOT:PSS, graphene nanopowder was mixed with the PEDOT:PSS ink solution [10]. Besides ink, there were other items that were prepared, such as ion membranes and substrates. A Dimatix material printer was used to print and fabricate the requisite systems and parts [10]. Printing was mainly done on wax patterned filter paper. Figure 2 shows the fabrication process of a potentiometric device. Electrical resistance was measured across the electrode traces. The devices that were created in this study were designed for observing sodium and potassium ions. Based on this study, inkjet printing appears to be a suitable method for creating different types of ion-sensing devices.

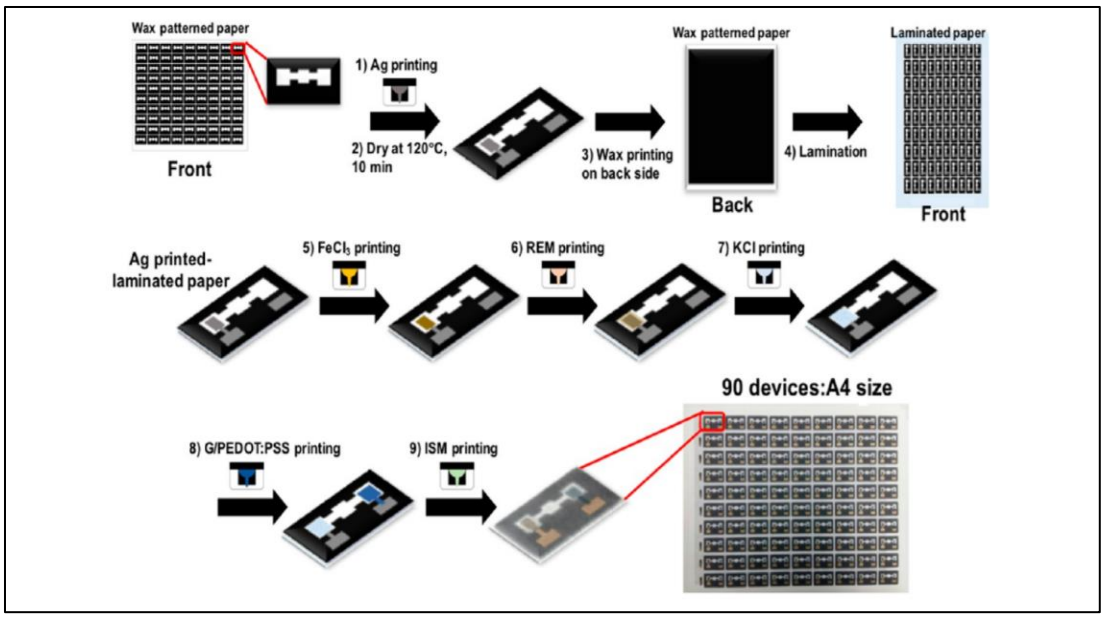

Figure 2. Potentiometric device fabrication process [10]

2.1.4 *Plate Wave Acoustic Sensor*

Inkjet printing was previously used in a study to create a plate wave sensor. Polyvinylidene fluoride (PVDF) was used as the substrate. A high temperature stretching procedure was used on the PVDF to make it piezoelectric. Electrodes were printed using an ink that has a mixture of PEDOT:PSS, DMSO, and Triton X-1000 [11]. A Microfab nozzle was used with the printer. The printing was done in an open environment, and a sponge was used so that the nozzle was as humid as possible. Each printing cycle consisted of three passes, and each of the sensors went through three cycles, for a total of 9 passes. This was done to reduce resistance. Adhesive copper tape was then put on the substrate. For results analysis, a Laser Doppler Vibrometer was used to look at standing wave measurements. Electrical measurements were made using a ADC/DSP data acquisition system [11]. In addition, the sensor was loaded with polyvinyl alcohol layers. This was done so that the sensor behavior can be looked at and compared to acoustic thin film theory. As it turned out, the sensor behavior matched the predictions based on the theory [11]. Overall, the study

describes a possible procedure for creating an all-polymer, flexural plate wave sensor using inkjet printing. Figure 3 below shows an image of the sensor in the study.

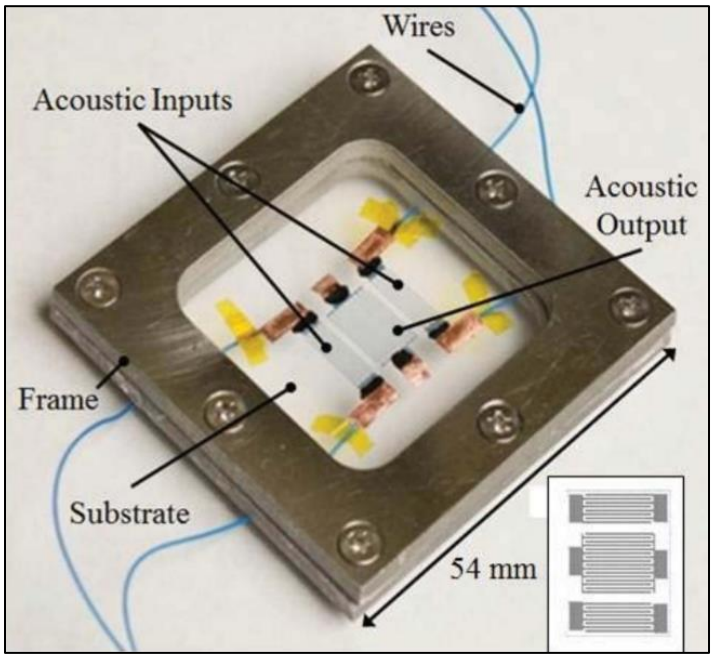

Figure 3. Completed sensor [11]

2.2 THERMAL IMAGING DEVICES

We looked at some of the previous work that has been done on thermal imaging devices. This allowed us to see some of the different ways in which thermal imaging devices can been developed and fabricated. In this section, we describe some of the work that we reviewed.

2.2.1 *Superconducting Bolometer For Fourier transform spectroscopy*

A superconducting transition edge sensor bolometer has been designed in the past for spectroscopy. The bolometer was made with a microstructured metal absorber and a transition edge sensor. The transition edge sensor was used for the thermistor. In terms of design, the structural size of the absorber was smaller than the smallest relevant wavelength. The absorber, which has a high and spectrally uniform absorptance in the spectral range from 0.1 THz to 3 THz,

was in the shape of a metal grid with a certain width and length. The thermistor was created in the form of a bilayer with layers of niobium, a superconducting metal, and aluminum. Niobium was also used to make and connect the leads to the transition edge sensor. For testing, the bolometer was operated in a helium bath cryostat [12]. A radiation shield was used to block any thermal radiation from the surrounding environment that may affect measurements or readings. Epoxy was used to blacken the interior of the radiation shield. Afterwards, the noise equivalent power of the bolometer was determined through various experiments. The linear response range of the bolometer was also looked at with the help of the Metrology Light Source, which is an electron storage ring that can generate coherent THz radiation [12]. A 3 THz long pass filter was used to block visible and infrared radiation. To evaluate the bolometer, a vacuum Fourier transform spectrometer was used to perform transmittance measurements. The measurements, along with other experiments done on the bolometer, showed that the transition edge sensor bolometer can successfully be used for Fourier transform spectroscopy. The bolometer has a highly linear response and dynamic range. Figure 4 below shows a prototype of the bolometer.

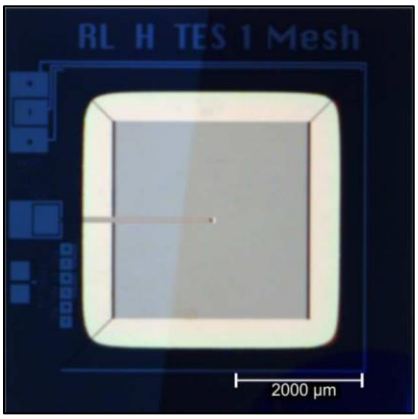

Figure 4. Transition edge sensor bolometer prototype. The thermistor is located in the center. The leads of the thermistor go to the left. The gray area represents the metal mesh absorber [12].

2.2.2 *Room Temperature Bolometer*

In a previous work, room temperature bolometers, which are highly common in IR cameras, were fabricated using a YBCO film. The YBCO film was created on a sapphire substrate through a pulsed layer deposition process. In addition, the YBCO film was shaped as a microbridge [13]. This bridge overlapped with a thick gold film spiral antenna. An SEM image of the bolometer at the antenna center is shown in Figure 5.

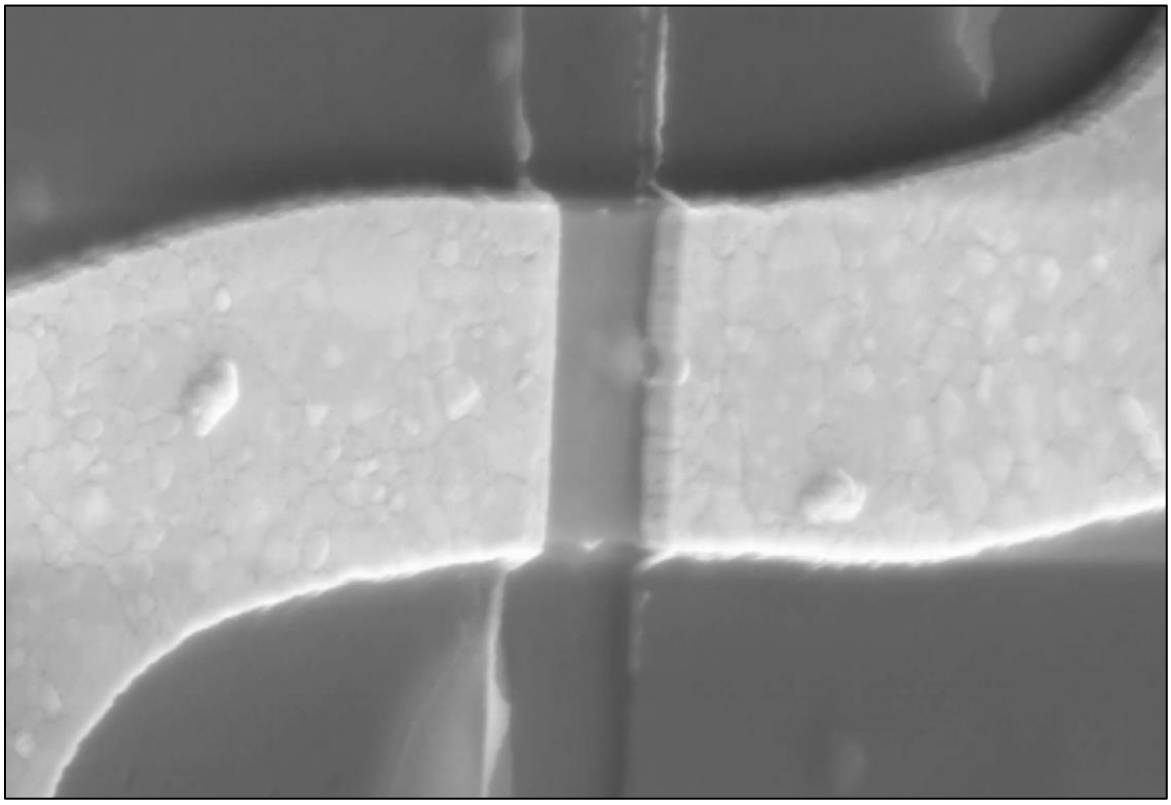

Figure 5. Bolometer at the center of the spiral antenna [13]

Three different bolometers, all of which had different areas between antenna pads, were tested. Signal sources were used for responsivity measurements. One of the variables that was looked at was the voltage responsivity. The voltage responsivity of the bolometers, shown in Figure 6, were both measured at room temperature and calculated based on the device parameters. For measurements, the bolometers were biased with a current that was constant. A lock-in

amplifier was also used to measure the noise voltage. As a whole, the results of this work showed that YBCO films can be promising when it comes to designing room temperature bolometers with fast response times. The size of the bolometers can also be reduced in order to reduce thermal coupling and improve sensitivity [13].

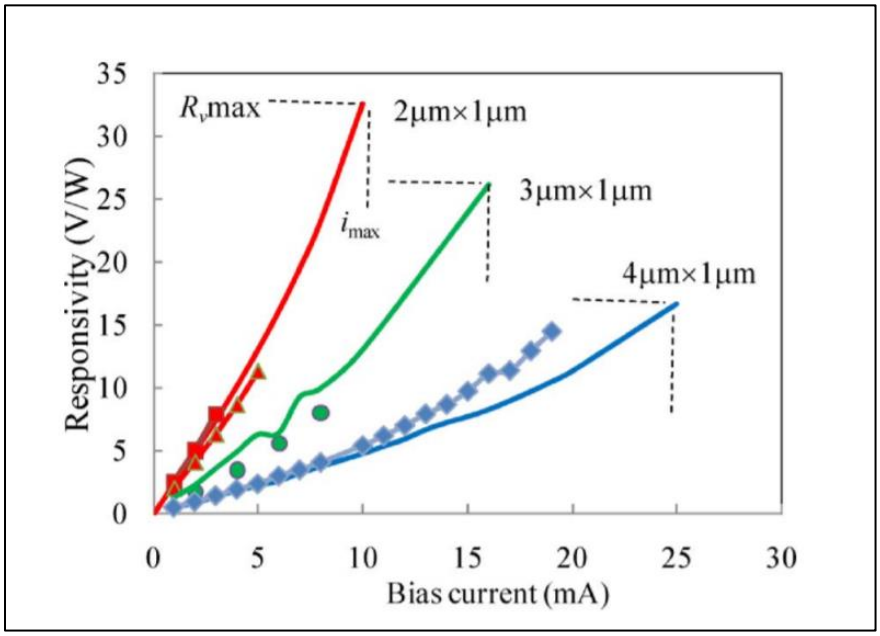

Figure 6. Voltage responsivity of bolometers. For each of the bolometers, the solid line represents the calculated responsivity and the symbols represent the responsivity that was measured [13].

2.2.3 *Pyroelectric Detectors with NiCr Thin-Film Absorber*

Pyroelectric detectors are devices that can be used for observing infrared radiation. These detectors can be created in a variety of different ways. In one instance, there was a design process that involved the use of nickel-chromium (NiCr) thin-film IR radiation absorbers. Single-element pyroelectric detectors were made using a polarized, monocrystalline $LiTa0_3$ wafer [14]. The $LiTa0_3$ was thinned down using mechanical and chemical-mechanical polishing methods. Electrodes were made of NiCr. A thin-film, high porosity nanostructure was made using oblique-

angle deposition and substrate motion [14]. This nanostructure was used to build the absorbers. A liftoff technique was used to pattern and deposit the absorber structures, shown in the SEM image in Figure 7, onto an area that is radiation-sensitive. The detectors that were built had different thin-film absorber thicknesses.

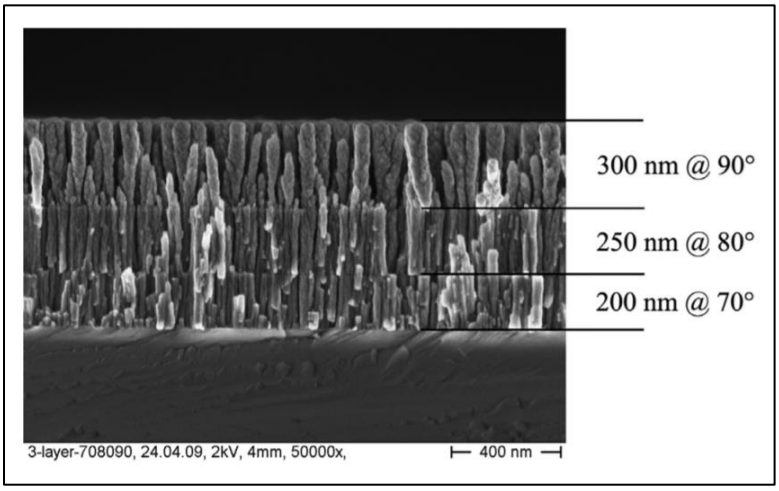

Figure 7. SEM image of a three-layer NiCr absorber structure deposited at varying angles of incidence [14].

The spectral responsivity of the detectors were looked at and compared between wavelengths of 1 um and 15 um. Figure 8 shows the spectral responsivity of each of the detectors. For each detector, the responsivity was normalized at 1 um.

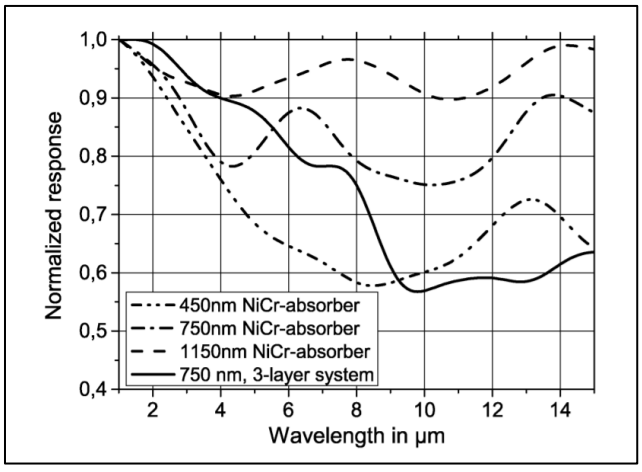

Figure 8. Spectral responsivity of the pyroelectric detectors [14]

The spectral responsivity of the pyroelectric detectors showed fairly good uniformity. The detector responsivities also showed that the absorptance can also be increased at higher wavelengths, depending on the film thickness.

2.2.4 *CMOS Microbolometers*

CMOS (Complementary metal-oxide-semiconductor) microbolometers were once designed through a standard CMOS process and a micromachining process. The microbolometers consist of suspended and serpentine distributed structures that have resistance. Serpentine structures were used in order to maximize the thermal resistance of the microbolometers. An SEM micrograph of a microbolometer can be seen in Figure 9. The microbolometers were built using CMOS process polysilicon and dielectric layers [15]. There were some areas in the microbolometers that were used for underetching. The silicon bulk was exposed in these areas through a CMOS process that included the use of no-glass, via, contact, and active masks. The suspended structures were micro machined through a dry process. Etching was done through RIE (reactive-ion etching) with no mask. A wet aluminum-etching step was used to remove metal residue. Afterwards, gold black deposition was used to enhance the absorption. Additional dielectric bridges were also added in order to improve the stability of the structures.

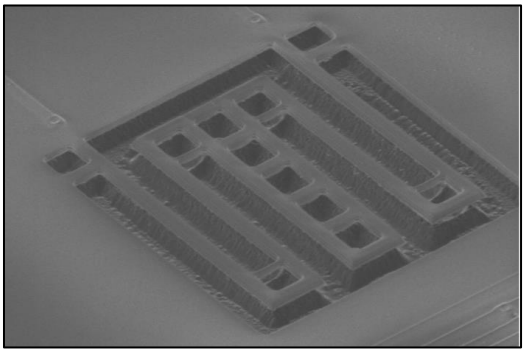

Figure 9. SEM micrograph of a serpentine structured microbolometer with additional dielectric bridges [15]

For the microbolometers, an oven was used to measure the resistance at certain temperatures. Figure 10 shows the resistance vs temperature plot that was obtained. In addition, the voltage response was looked at and showed good linearity. The responsivity can be improved by using polysilicon layers that have a higher temperature coefficient of resistance.

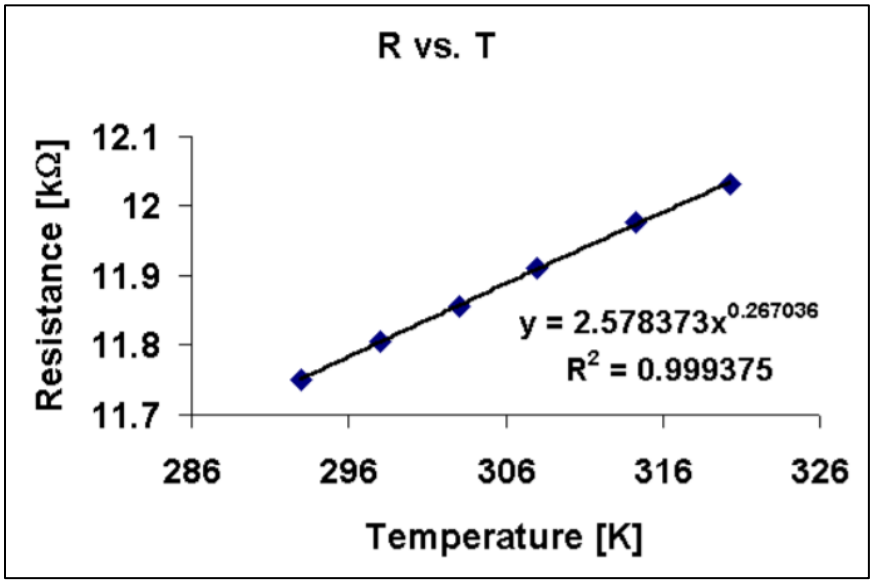

Figure 10. Resistance vs temperature plot [15]

2.2.5 *High-Responsivity Thermoelectric Infrared Detector*

A thermoelectric IR detector was created using an IR absorber and a polysilicon-based thermocouple, along with other materials. The thermoelectric IR detector was uncooled, so it generated electrical signals based on absorbed photons and heat. The most significant component of the detector was the thermoelectric material, which is used to detect the difference between the absorber temperature and the ambient temperature [16]. In terms of structure, the IR detector consists of an absorber that is shaped like an umbrella and thermoelectric wires below it. A suspended membrane and post are used to hold the absorber in place. Figure 11 shows the detector structure with components labeled.

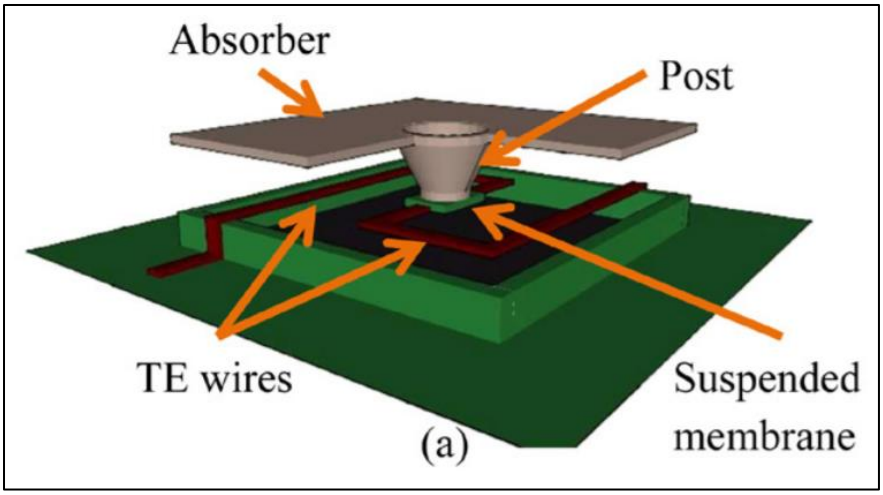

Figure 11. Thermoelectric IR detector structure [16]

The main goal of the absorber was to absorb all incoming radiation within a certain bandwidth. Silicon nitride was used as a dielectric material. During the detector fabrication process, a plasma enhanced chemical vapor deposition system was used to create small oxide islands on a silicon wafer [16]. Polysilicon thermoelectric wires were also deposited. An AJA sputtering system was used to sputter tungsten, which was used as the contact material. A parylene layer was used to cover the thermoelectric wires. The absorber was deposited layer by layer. A nichrome layer was initially sputtered. Afterwards, a dielectric silicon nitride layer was deposited and then the top metal layer was sputtered. The top metal layer also consists of nichrome. After fabrication, the detector was evaluated. A detector was placed in a vacuum chamber so that the voltage of the detector can be recorded. The output voltage of the detector was recorded in order to determine the responsivity of the detector. The responsivity of the detector is the output voltage divided by the input power. Furthermore, the responsivity of the detector was looked at under different chopping frequencies. Figure 12 shows the measured responsivity at different frequencies and compares the measured responsivity with a responsivity model. A digital oscilloscope was

used to determine the detector noise. Based on the results, the detector has high responsivity and detectivity.

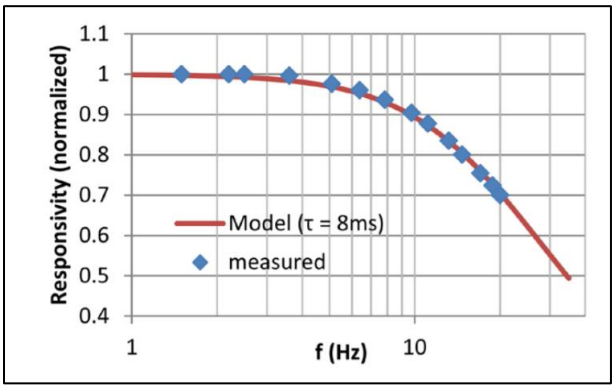

Figure 12. Responsivity vs chopping frequency [16]

2.3 Thermal Imaging Device Comparison

The studies that were looked at for this research were used to compare different types of thermal imaging devices. Table 1 shows a comparison between each type of thermal imaging device.

Table 1. Thermal imaging device comparison chart

Thermal Imaging Device Type	Dimensions & Sensitivity/Responsivity	Materials & Manufacturing Techniques	Advantages & Disadvantages
Bolometer	• Bolometer area can be around (6.6 by 6.6) mm^2 • Wide range of sizes for bolometer • Sensitivity can range from 0.06 to 10 Ω/K	• Aluminum • Silicon • Pulsed layer deposition • Reactive ion etching	• Excellent sensitivity • Requires time-consuming clean room process to manufacture • Amplifier or filter may be needed to enhance and read output
Thermoelectric Device	• Device size can be extremely small (around 100 um by 200 um in area) or extremely large (50.8 mm by 50.8 mm) • Responsivity can range from 200 to 1800 V/W	• Silicon • Bismuth telluride • Surface Micromachining • Wet etching	• High detectivity and/or responsivity • Short working distance
Pyroelectric Device	• Wide range of sizes for pyroelectric devices • Radiation can be looked at between a wavelength range of 1-15 um • Responsivity can range from 1 to 10 V/W	• Nickel-chromium • Zinc Oxide • Photolithography • Chemical vapor deposition	• Broadband • Short working distance • Responsive to vibration depending on how the device is built

We used inkjet printing to create a polymer-based resistive thermal imaging device that has a simpler design and higher sensitivity compared to imaging devices in previous studies. The fabrication process for our device is much cheaper than additive manufacturing processes. In addition, amplifiers and filters are not needed in order to see the resistance change across our device. The imaging device that we designed does not have the disadvantages of traditional thermal imaging devices. Details about our resistive device are shown in Chapters 4 and 5.

Chapter 3. INKJET PRINTING SYSTEM

An inkjet printing system was used to print the resistive thermal imaging device. The inkjet printing system consists of three main subsystems: the jet head, DAQ, and the stage and motion control. Generally, the ink or liquid is initially placed in the reservoir and clamped shut. During a print, the amplifier and data acquisition system are used to send a signal to the motion controller and jet head. This signal actuates the system and forces droplets to come out from the head at a constant rate. The printing system is summarized in Figure 13. This chapter goes into detail on the main devices that make up the inkjet printing system, as well as the ways in which the devices are connected to each other. In addition, this chapter describes the programs and software that are involved in the system.

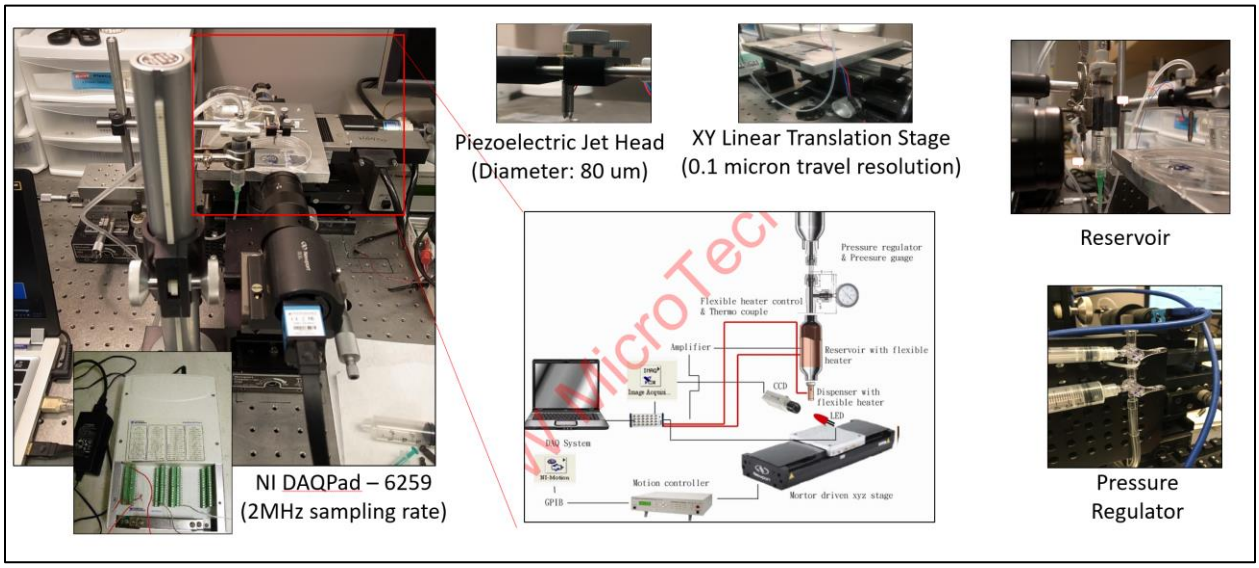

Figure 13. Printing system summary with major components

3.1 JET HEAD AND AMPLIFIER

The jet head is used to dispense ink on a surface and print soft electronic circuits and devices. The jet head has two terminals, positive and negative and needs around 30 volts to get

actuated. Moreover, the drop size from the jet head depends on the waveform signal given to the jet head. The high voltage requirement of the jet head sensor necessitates the use of a power amplifier that takes a small input voltage (waveform) and amplifies it for the jet head. This power amplifier is a single input single output amplifier that requires an external AC power supply.

The jet head that was used for printing was purchased from MicroFab Technologies. The head that was used has a diameter of 80 um. Figures 14 and 15 show an image of the jet head and the power amplifier that was used, respectively.

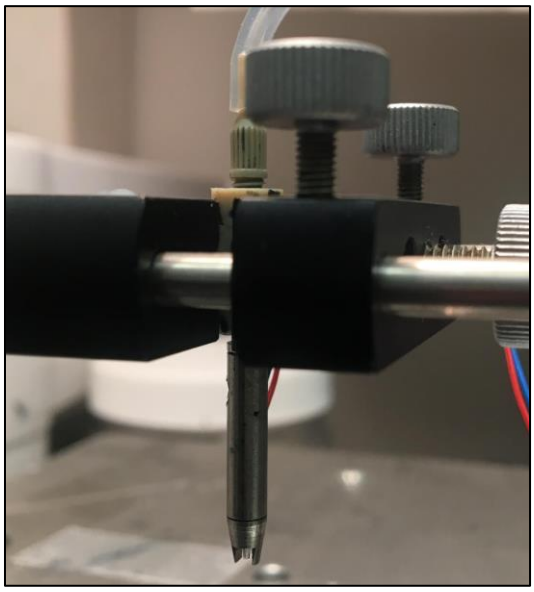

Figure 14. Jet head

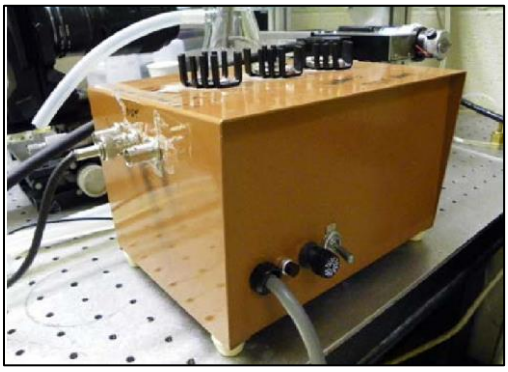

Figure 15. Power amplifier

3.2 STAGE AND MOTION CONTROLLER

There are two stages, UTM50CC-.5HA and UTM50CC-1HL that are used for the movement of the surface on which the pattern is to be printed. One of the stages is used for movement in the x direction, and the other stage is used for movement in the y direction. The resolution of the "x" stage is 0.5 micrometers and the resolution of the "y" stage is 1 micrometer. The stages, shown in Figure 16, are DC motor driven and are controlled by a motion controller. In terms of accuracy, the stages have a 0.1 micron travel resolution, which means that the stages can move in increments of 0.1 um.

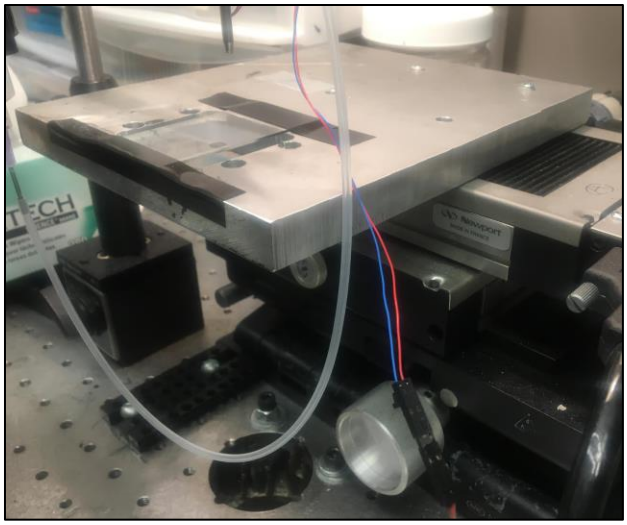

Figure 16. Linear translation stages

The controller that we used was Newport Motion Controller ESP 300, which is shown in Figure 17. The motion controller uses a GPIB card and has a minimum frequency of 1 Hz. Each stage is connected to the motion controller by a D connection. The controller is connected to each of the x and the y stage under the printing surface. These stages are simultaneously controlled by the controller although the movement is restricted to one stage at any given time. The motion controller is connected to the computer using a GPIB-USB cable and communicates to the LabVIEW via serial port. The LCD interface on the motion controller tells the exact position of

the active stages. It also tells what stages are on at a given instant of time. One can also set PID control parameters by going to its associated software installed in the computer.

Figure 17. Newport Motion Controller ESP 300

3.3 Data Acquisition System

The data acquisition system is one that can be used to control certain signals and variables, such as the voltage. One of the devices that we used for data acquisition was the NI DAQPad – 6259, a hardware product from National Instruments. This product, shown in Figure 18, is a state of the art data acquisition device that has 32 Analog Input channels and 4 Analog Output Channels. Only two of the four analog output channels are utilized in the inkjet system, one for the jet head and one for the LED strobe light, which can be connected to the DAQ analog output and is shown in Figure 19. The Analog Output (AO) channels can give a voltage between +-10V and a maximum current of 10 mA. The voltage waveforms are generated in LabVIEW for the jet head and the LED strobe light. Two input terminals of the power amplifier are connected to the AO0 and AO GND. The power amplifier has its output connected to the jet head. Thus, the power amplifier is used to give a 30V voltage signal to the jet head through the DAQ. The LED strobe set up is connected to

the AO1 and AO GND. The LED strobe blinks when the system is actuated. The DAQPad requires an external AC power supply and is also connected to the computer processor by a USB cable. This USB connection establishes the contact between LabVIEW and the DAQPad-6259.

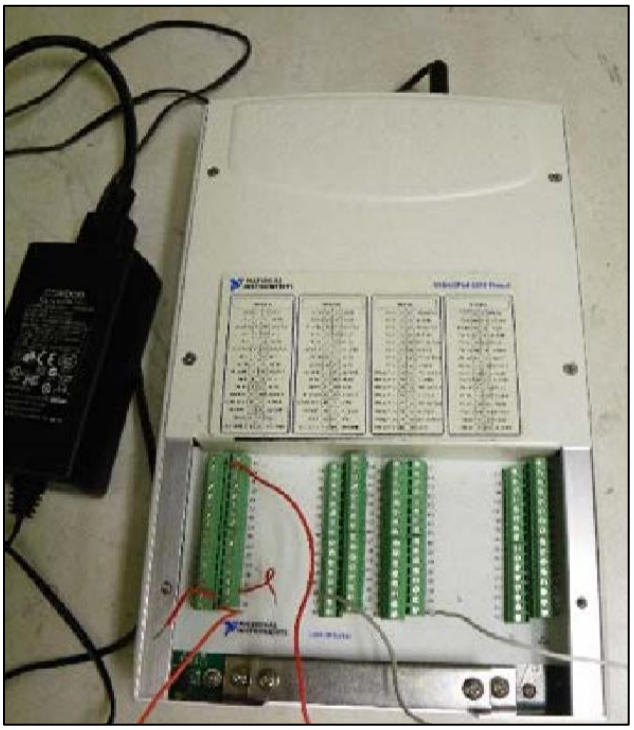

Figure 18. NI DAQPad – 6259

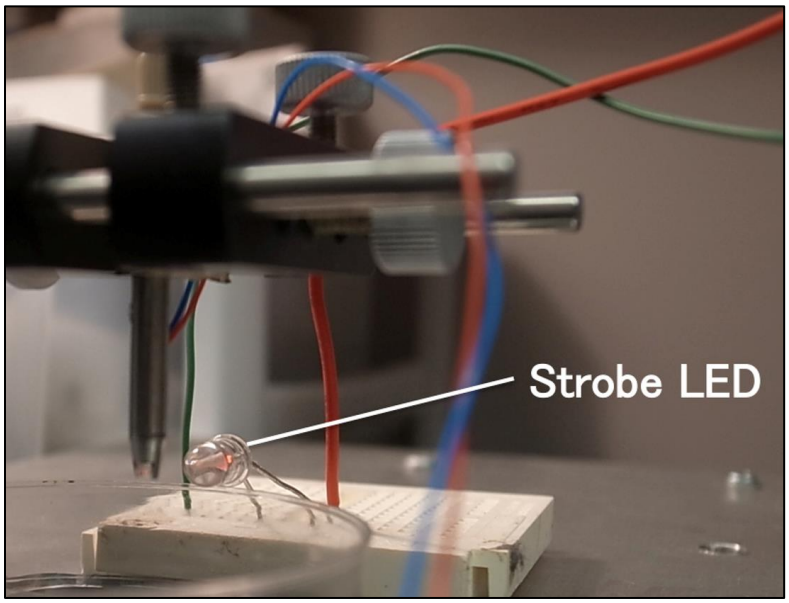

Figure 19. LED strobe

3.4 INKJET PRINTING SYSTEM SET-UP

The inkjet printing system was put together through multiple steps using the devices described above and in the previous pages. One of the steps involved clamping the jet head so that it does not come loose during printing, as shown in Figure 20. The plastic tube that is attached to the jet head was connected to the reservoir, shown in Figure 21, where the ink or substrate is placed prior to any print.

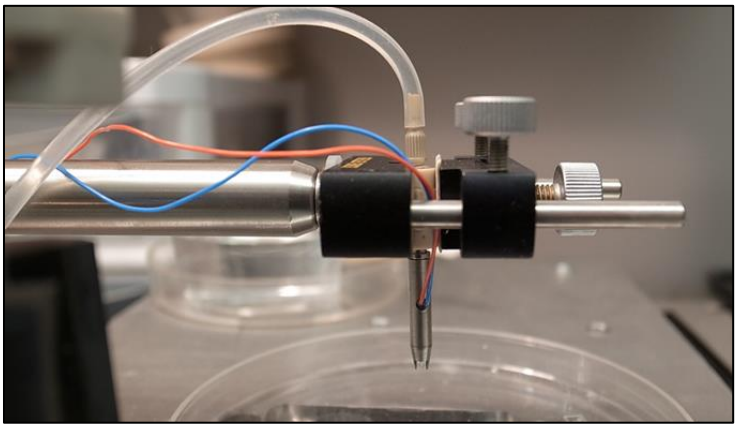

Figure 20. Jet head after clamping

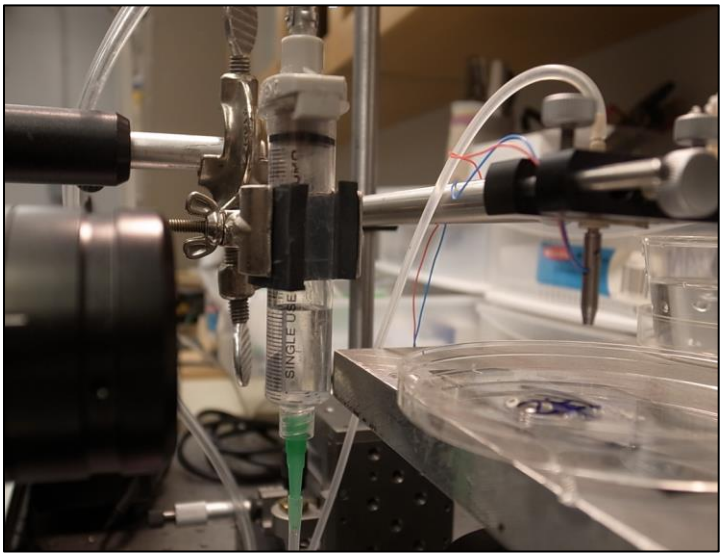

Figure 21. Reservoir

The pressure in the reservoir can be controlled through a pressure regulator with valves, shown in Figure 22, that can be used to allow air to move in certain directions. The pressure regulator is there because if there is too much or too little pressure, the jet head will not dispense any liquid or substrate even if there is actuation. The pressure in the reservoir can also be controlled by moving the reservoir up or down. Ideally, the liquid in the reservoir should be around the same level horizontally as the jet head tip. As shown in Figure 20, there is a red wire and a blue wire attached to the jet head. These wires were connected to a set of amplifying wires that are connected to the DAQPad. These wires are responsible for transferring electrical signals that cause actuation. This actuation then leads to a drop of ink or substrate being dispensed. The amplifier input was connected to the DAQPad output, shown in Figure 23. It is important to make sure that the wire connections are correct, so that there are no issues such as shorting.

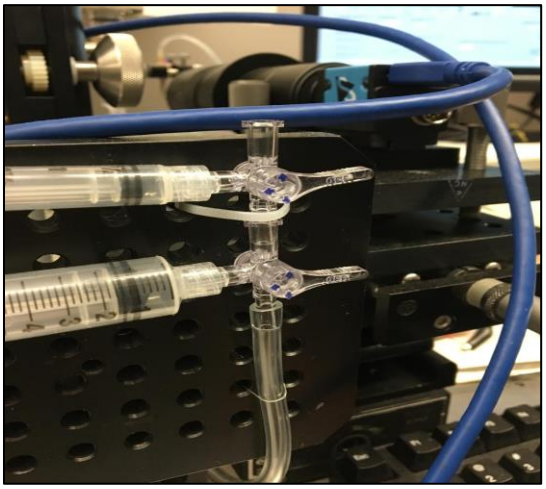

Figure 22. Pressure regulator valves

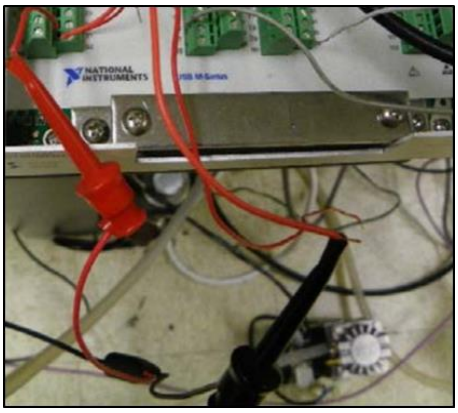

Figure 23. Amplifier connections. The red clip of the amplifier connects to the analogue 0 of DAQPad and the black clip connects to the ground.

As for the motion controller, it is connected to the main computer through a parallel cable. The DAQPad is attached to the same computer via USB cable. Additionally, we mounted a USB microscope camera near the stage so that we can monitor the jet head closely during any print. Figure 24 shows the camera setup, and Figure 25 shows a section of an inkjet printing system after the devices are put together.

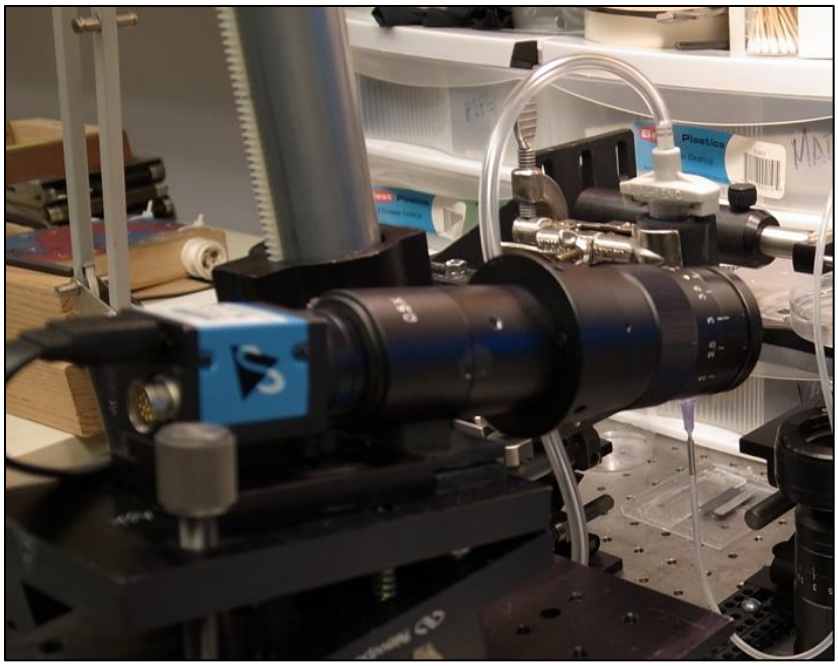

Figure 24. Microscope camera set-up

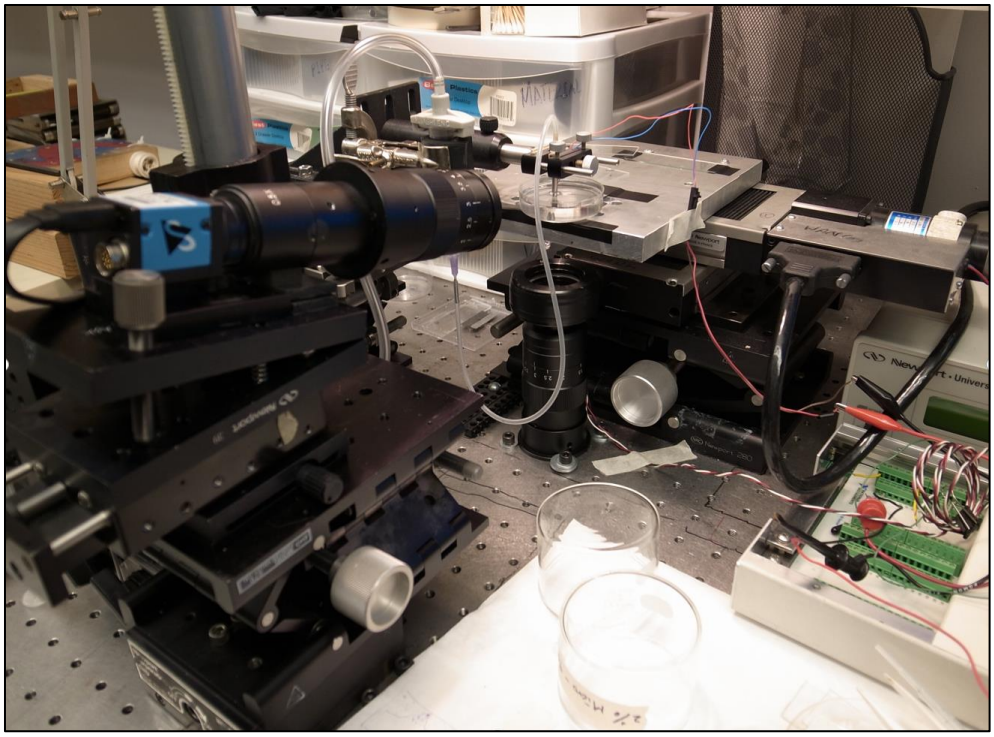

Figure 25. Inkjet printing system with the devices connected and organized

3.5 SOFTWARE COMPONENTS

The inkjet printing software consists of a number of different modules and components. Specifically, the programs and the software interface were developed using LabVIEW 8.6. LabVIEW is a GUI based programming environment where each input and output is represented on the front panel and the block diagram. The front panel of the LabVIEW program developed for this system is the user interface of the program. This is the user console from where a user controls the execution of the system and can vary the input parameters. The interface is tab bases and each module has its controls and indicators (both numeric and graphical) in their respective tabs.

The software starts with an input image that is processed in the pattern processing software. Depending on the required length of the pattern this module returns the position array which contains x and y positions in the 2-D space where inkjet needs to print. Waveforms for the inkjet

and the LED strobe light are generated in the second part of the program. The waveform of the inkjet decides the drop size. After the generation of the waveforms, the position array, or the x and y coordinates generated in the previous step, is used to control the motion of the stage. In every iteration, the stage moves to the next point in the array and inkjet is actuated by giving the signal to the DAQPad. Also, the LED strobe light switches on depending upon the parameters set in previous step. This is the third part of the program. This iteration continues until all the position elements are printed.

The inkjet printing software is made up of three main modules: the pattern generation and processing module, the waveform generation module, and the stage and motion control module.

3.5.1 *Pattern Generation and Processing Module*

The pattern generation and processing module imports a selected Bitmap image into the memory buffer allocated at the start of the program. The image is then converted into binary image using a selected value of threshold. The software calculates the pattern size in pixels using the characteristic length of the desired pattern to be printed. The new pixel size is calculated using the resizing module that has been modified for better accuracy. The software converts the resized image into pixel array where printing of dots is required. This pixel array is then converted into a position/distance array and then fed to stage control. Figure 26 on the next page shows a screenshot of the module.

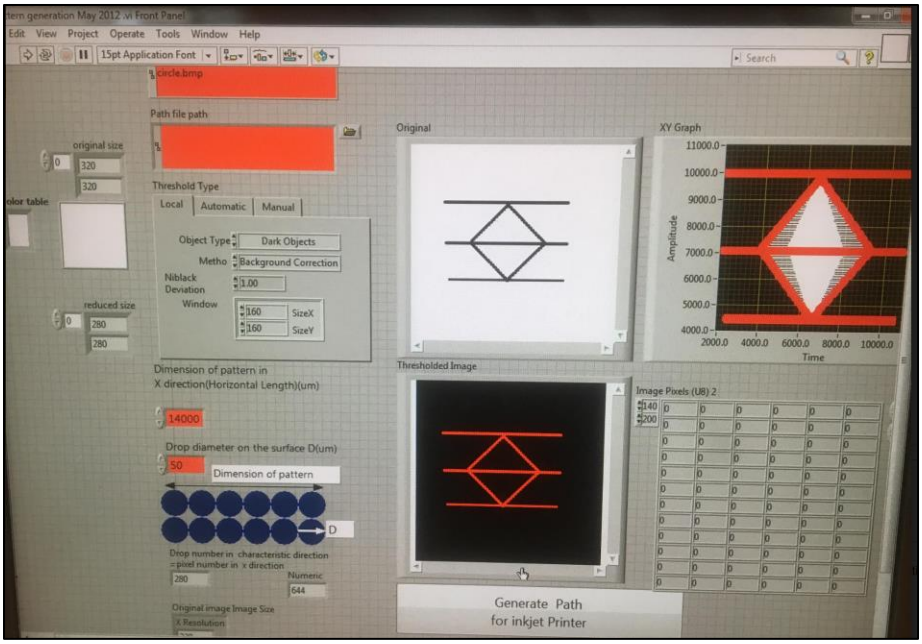

Figure 26. Pattern generation and processing module

This module is programmed using stacked structures in LabVIEW. The first stacked structure (call it A) in the block diagram is for the Pattern Processing. In the first stack of the structure (A0), temporary memory locations are created for the original image that will be called from the directory and its binary result after threshold has been applied to it. Figure 27 below shows a snippet of the LabVIEW diagram for this part.

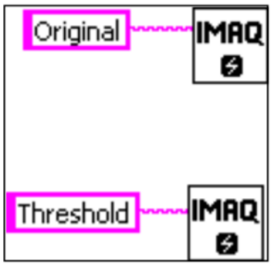

Figure 27. Pattern generation and processing module LabVIEW block diagram

After the space for the images is created in the memory, a while loop is initialized which terminates at the end of the Pattern Processing module. This while loop is initialized in the second stack of the stacked structure A and let it be A1. Another stacked sequence structure (call it A1A)

is initialized in the while loop and in the first stack of this sequence structure (call it A1A0), the image called from the memory is measured for its size.

After A1A0, there is a second sequence structure, A1A1. In this structure, image is converted into a binary image first. This is done in a case structure, the case selection of which is done from the front panel. The cases are names as “Local”, “Automatic” and “Manual”. They use IMAQ Local.vi, IMAQ AutoB threshold.vi and IMAQ Threshold.vi. These .vi s are there in the IMAQ toolbox. Any of these threshold methods can be selected from the tab selection. After the image is converted into the binary image, the binary image is converted into a 2D array using IMAQ ImageToArray.vi. The scaling factor is then calculated using the drop size and the characteristics length of the pattern to be printed in the x direction. Rounding off operation is also performed in case the need arises. The following code, shown in Figure 28, provides the calculation of the scaling factor.

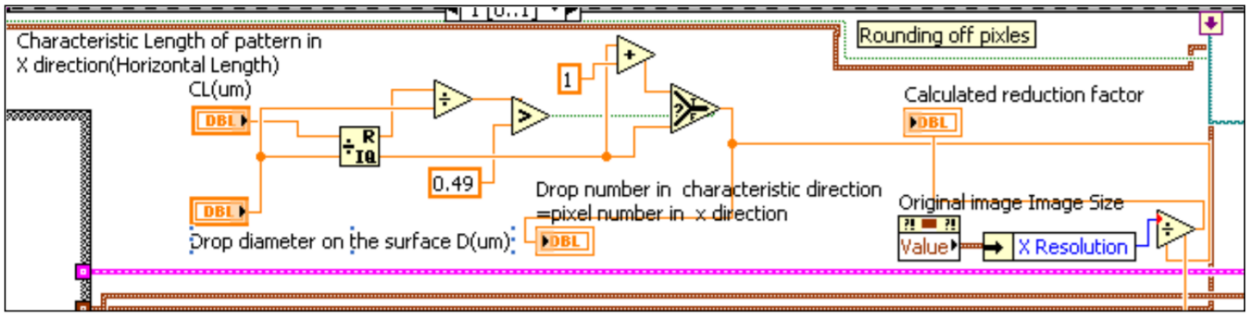

Figure 28. Scaling factor code in LabVIEW

After calculating the scaling ratio, which can be a floating point number, the image is resized using a nested for loop algorithm. This algorithm replaced an older version of the scaling algorithm that could only take integer scaling ratios and was very inefficient. At the end of this algorithm the scaled image matrix is converted to a scaled image called an “RS Image”. This image and its size is shown on the front panel. After this operation has taken place, the user has to trigger the start of next steps by clicking “Stop and generate position and path for the inkjet printer”. After

this button is pressed, the while loop terminates and the control reaches the third stack of the stacked sequence structure. In the third stack, the images are destroyed and the memory location is freed.

In the fourth and the final stack of the stacked sequence structure for Pattern Processing, the rescaled image pixel array calculated in the second stack after the scaling algorithm is used for further processing. This pixel array is already a binary array as it was obtained after scaling a binary image array. Now, 1s are searched in this rescaled pixel array using search_2D_array.vi. This vi gives the indices of all the elements which have 1. This means the resultant array is the group of pixel position where 1 is present in the rescaled image or where printing needs to be done. "Indices" show the resultant array out of the array search operation. The Next part of this algorithm is used to translate or flip the y axis by multiplying by -1 and adding the number of rows. The resultant x and y positions are built to form an x position matrix and a y position matrix. These matrices make up the position array that is used by the stage control module.

3.5.2 *Waveform Generation Module*

In this module, waveforms are generated for the jet head and for the LED strobe light. Waveforms are generated based on parameters that can be defined by a user, such as the jet head actuating intensity voltage and waveform time. Like Pattern Processing module, this module also has a stacked sequence structure programmed. The stacked sequence structure has two stacks. The first one opens a reference to itself using its own path and Changes the current values of all controls on the front panel to their defaults. The reference invokes an error if conditions are not matched. In the second stack, jet head waveform generation takes place using waveform generation subvi.vi. This sub vi takes all the parameters from the front panel of the Waveform Generation module and

uses them to come up with the waveform for the jet head. Figure 29 shows a part of the waveform generation LabVIEW code.

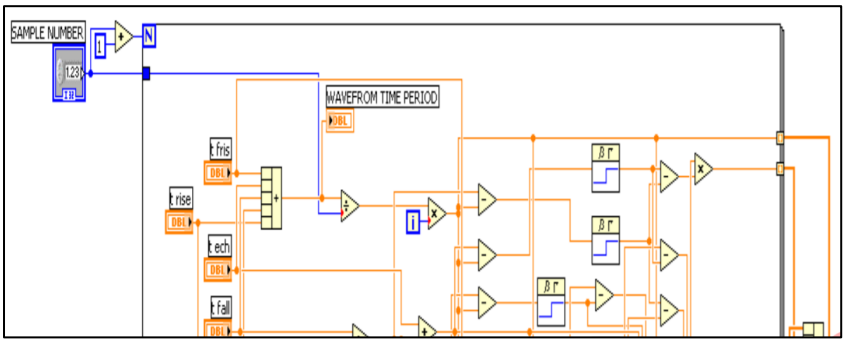

Figure 29. Waveform generation LabVIEW code

The waveform constructed using the sub vi is then graphically indicated on the front panel under Waveform Generation >> Pulse control. In the current stack, waveform for strobe light LED is also constructed using an excel sheet of data points. The two waveforms are matched in the time domain. A delay control present in the front panel under Waveform Generation >> Inkjet Driving Waveform control is used to alter the delay in the strobe light actuation and sensor actuation. It is sometimes necessary to play with this delay to observe the drop using stroboscope. Both the waveforms are mux-ed together and sent out for DAQ assistant and to be used in last stages of the program. In the last part of the current module, Waveform Generation, the axis number and addresses for the motion control device is initialized.

Waveform generation is divided into two tabs, Pulse Control and Inkjet Driving Waveform Control. The Pulse Control tab controls the waveform for the inkjet head. The waveform developed in this tab is used to actuate the piezoelectric sensor present in the jet head. Another control, “Delay between drop and stage” is present on the front panel and has a default value of zero. This delay value is in milliseconds and controls the delay between the printing of the drop and movement of

the stage. The graphical indicator shows the waveform formed out of parameters specified. This waveform is given to the AO0 of the DAQmx in the third and the last part of the program.

The Inkjet Driving Waveform Control tab controls the waveform for the strobe light. There is a control to select a Microsoft excel file that contains data points for the strobe light. There is another control set up to tune the timeout in seconds for the DAQ assistant. The gain of the amplifier is a physical property of the power amplifier in use and hence should be kept at 30 if the same amplifier is used. Some of the indicators that are present on the front panel here are waveform graphs for strobe light (left) and combined graph for strobe and jet head actuation waveform (right). Some other indicators are also present on the front panel and are related to mathematics involved with the samples of the waveform and time interval of the waveform.

3.5.3 *Stage Control Module*

The stage control module takes the outputs of the other two modules and prints the substrate on a specified surface by moving the stage on which the surface is attached (using the position matrices from the pattern generation and processing module) and by printing at correct points in the 2 dimensional physical spaces (using waveforms from the waveform generation module).

The stage control works in the following way. Form a current position it goes to the next position moving x and y stages in a fixed order. The stages never move simultaneously. Hence, distance in x direction is traversed first, and then the distance in y direction is traversed. The stage starts from rest to motion with some acceleration, then maintains a constant velocity and then when it is about to reach the destination point, it decelerates. The user can specify the Acceleration, Velocity and Deceleration values for each of the x and y stage from the front panel. These values are initialized in a For loop. This for loop is the mother loop in this module. Every operation takes place under the For loop and the number of time for loop executes is the number of points where

printing needs to be done. Inside the For loop, a stacked sequence structure of 4 sequences is initialized. In the first sequence structure, the acceleration, velocity and deceleration values are sent serially to both the axis of the motion controller using the ESP-300 library function. A part of the LabVIEW code that does this is shown below in Figure 30.

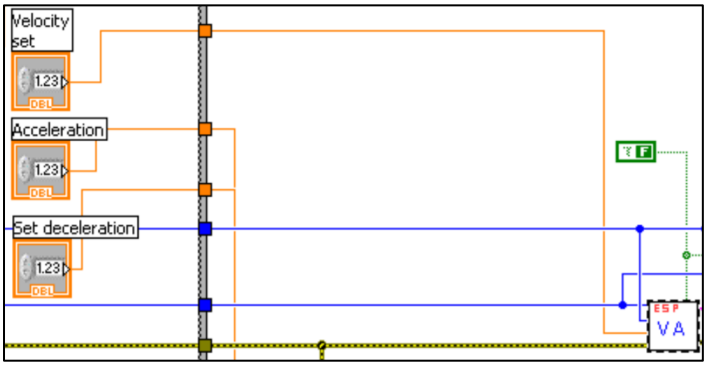

Figure 30. ESP-300 library functions code

In the second stack, the x position array and y position array obtained from module 1 (pattern generation and processing) are indexed one by one and are sent to the motion controller serially using the following code snippets. It is noted that in False condition is hard wired to the case structures for both the axes and hence the code snippet on the left is almost always executed. This code takes the indexed values of the x and y position arrays and moves the respective stages to these positions. These positions are no longer pixels and are actually physical units of distance (mm). In the third stack, the position of each stage is read back in a while loop and plotted on a graphical indicator. These values are compared with the reference values of x and y. The tolerance for the x and y values are checked. Figure 31 shows a part of the code that is responsible for this.

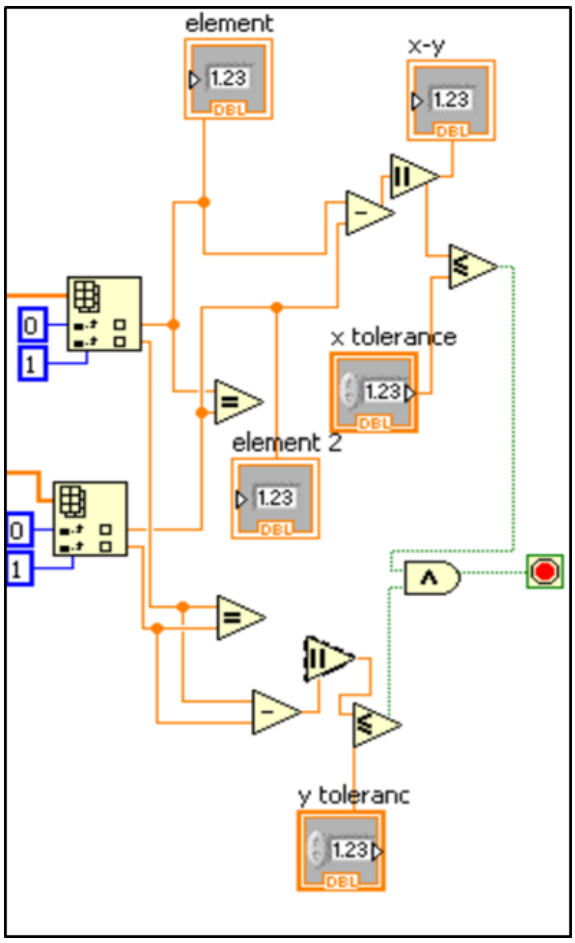

Figure 31. Checking the tolerance in the X and Y directions

If the x and y values exceed the tolerance level specified by the user, the while loop terminates and reaches stack 4. If the difference is under the specified tolerance level, the program control reaches stack 4, the last stack of the For loop. In this stack, the DAQ assistant takes in the mux-ed waveforms for the jet head and the LED strobe and sends it to the AO0 and AO1 channels of the DAQ card respectively. Figure 32 shows a part of the code that is responsible for jet head actuation.

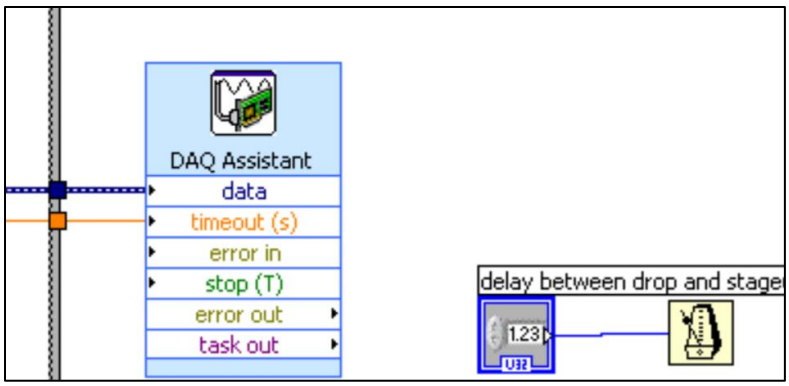

Figure 32. DAQ assistant actuating the jet head and the LED strobe

The sensor actuates and prints. The For loop continues to move the stages and print until the last point is reached, after which the program stops.

Chapter 4. RESISTIVE THERMAL IMAGING DEVICE DESIGN

In order to print and design the resistive device, we first had to determine the substrate on which the device would be printed on. We chose to print on PDMS (polydimethylsiloxane). PDMS is a chemically inert and thermally stable silicon elastomer that is commonly used in applications such as biomedicine [17]. PDMS can also exhibit hydrophobic properties that allow certain materials to build up instead of dissolving. In addition, we looked up a number of different conductive inks that could be used for printing. We decided to use Clevios PH 1000 (PEDOT:PSS) due to its cost, low viscosity and high conductivity. PEDOT is a polymer with a polystyrene base. Properties of the Clevios PH 1000 are shown in Table 2. When printing, we made sure to focus heavily on the pattern resolution rather than the print speed. A high resolution pattern can take a long time to print. Therefore, the patterns that we printed took a fair amount of time. This chapter describes the printing that was done in order to fabricate a resistive thermal imaging device.

Table 2. Clevios PH 1000 properties

Size (mg)	**Viscosity (mPas)**	**Conductivity (S/cm)**
100	15-50	850

4.1 PRINTING A COLUMN

Before any printing was done, we cleaned the jet head and the reservoir thoroughly using a combination of DI water, isopropyl alcohol, and micro-90 solution. Clogging is something that can happen frequently if dust particles and substrates are left in the jet head too long. Once the jet head was cleaned, we poured refrigerated PEDOT into the reservoir and let the PEDOT run to the tip of the jet head. Once the PEDOT reached the tip, we used the pressure regulators to close the

system and prevent the PEDOT from dripping on its own. When the system is closed, the PEDOT will only drop from the jet head when there is actuation from the data acquisition system. The jet head can be monitored closely using a microscopic camera and IC Capture 2.4, which is an image acquisition software. Figures 33 and 34 show an image of a clear jet head and an image of a jet head with the PEDOT at the tip. The images were obtained through IC Capture.

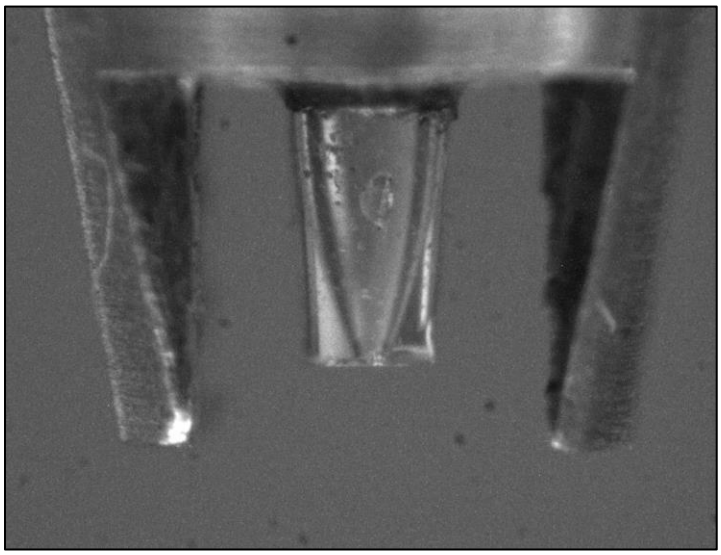

Figure 33. Clear jet head

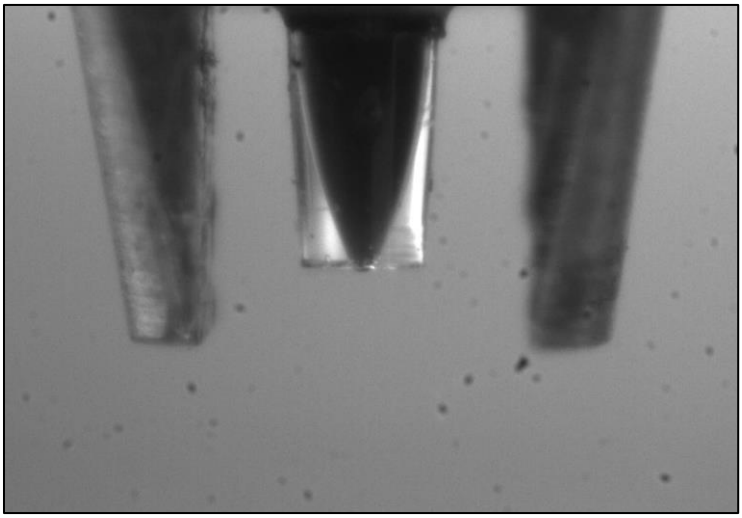

Figure 34. Jet head with PEDOT at the tip

In order to test out the printing system, we tried to print a straight column on top of a glass slide that was coated with PDMS. We put the glass slide about an inch below the jet head. A column pattern was generated through the pattern generation module and used by the stage control module. The delay time between drops was set to 100 milliseconds. However, a column did not build up. Through multiple print runs, we found out that the delay time between drops should be between 2-6 seconds. This is because the PEDOT drops need time to dry once it hits the PDMS surface. The PEDOT comes out as a liquid, so if the PEDOT does not dry between drops, a puddle forms. Therefore, we set the delay time between drops to 3 seconds, and ran the inkjet printing software to successfully print a column. The column was made of about 300 drops of PEDOT. Figures 35 and 36 show the column at different stages of the print.

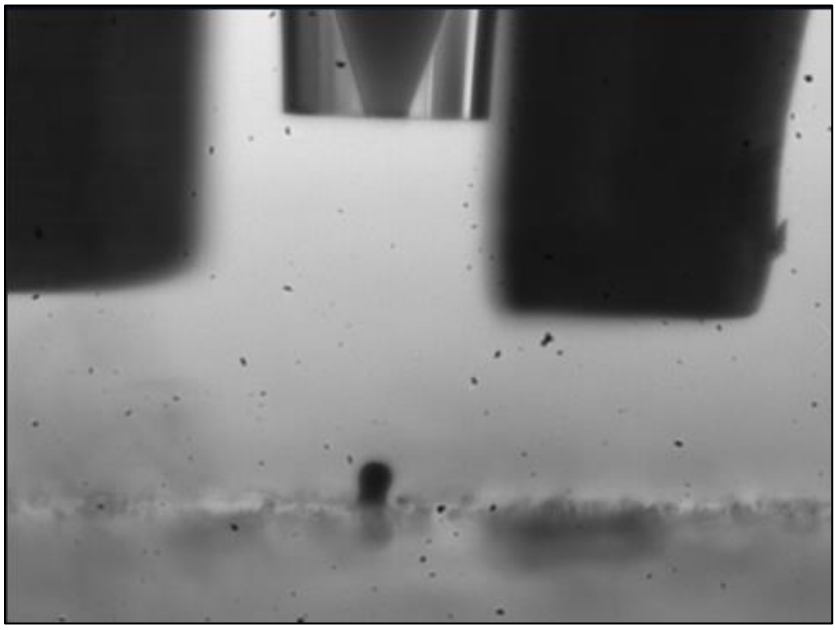

Figure 35. PEDOT column at the beginning of the print

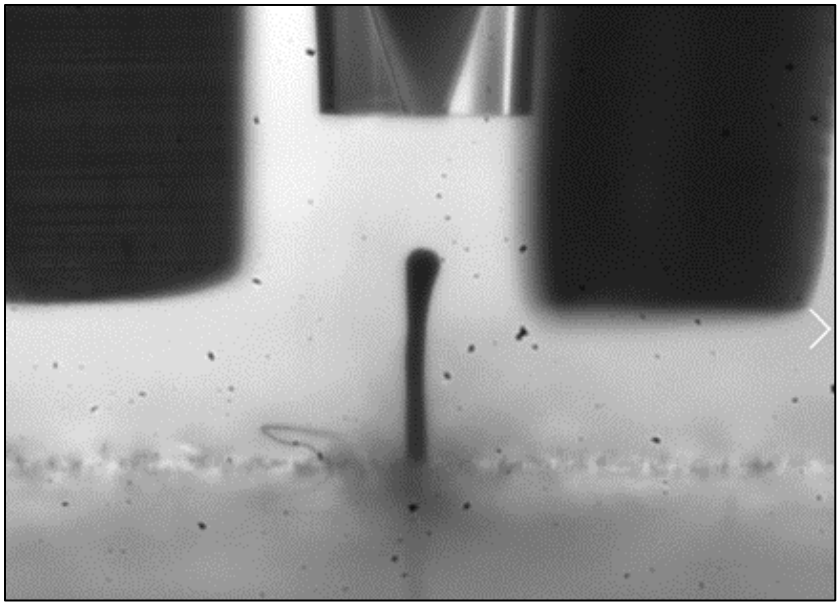

Figure 36. PEDOT column after 200 drops

The height of the printed column is about 5 mm. Printing the column allowed to verify the hydrophilic properties of the PDMS. We were also able to make sure that the entire inkjet printing system functions properly.

4.2 Design and Fabrication Of Imaging Device

The performance of a device can be assessed based on its sensitivity. The resistance of the sensing area is directly proportional to the length of the sensing area or circuit. This is based on the equation R = pL/A, where p represents the resistivity of the material, L represents the length of the path in the sensing area, and A represents the overall sensing area. Because of this, it is important to create a pattern for the device that is long in the sensing area. Before printing any pattern, we used ANSYS simulations to compare the resistance change across certain patterns and optimize the single cell device design. In the simulations, a current of 1 mA was applied across each pattern. PEDOT material properties were applied to the patterns. Each pattern was given a

thickness of 50 um. The voltage difference across the device was calculated through the simulations and used to compute the resistance. Simulations were also done with the patterns heated above room temperature so that the resistance change can be calculated. Figure 37 shows the patterns that were tested in the ANSYS simulations.

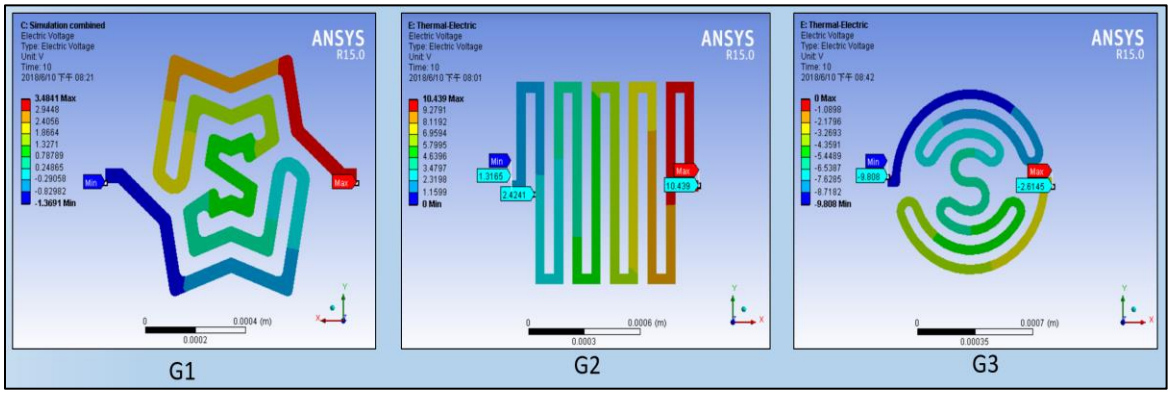

Figure 37. Patterns tested in ANSYS simulations

Table 3 below shows the characteristics of each geometry that was tested and the corresponding resistance change per device temperature from the simulations.

Table 3. Results from each tested geometry

Geometry	**Initial Resistance (MOhms)**	**Resistance after Joule Heating (MOhms)**	**Final Resistance after temperature increase (MOhms)**	**ΔR/ΔT (MOhm/ºC)**	**Temperature coefficient of resistance α (%R change/ºC^{-1})**
G1	5.116	5.094	4.853	- 0.044	- 0.009
G2	9.254	9.123	8.779	- 0.074	- 0.008
G3	7.215	7.194	6.890	- 0.059	- 0.008

Based on the simulations, geometry 2 produces the highest resistance change per change in device temperature. Therefore, in order to maximize the sensitivity of the device, we created a

zig zag print pattern similar to the pattern used in the simulation. We also decided to use the zig zag pattern for our device because the inkjet printing software has trouble processing curved paths. Specifically, the pattern generation and processing module/program seems to convert circular paths into steps of lines. As a result, we used the zig zig pattern. In terms of the device design, the zig zag pattern is sandwiched between two contact pads. Figure 38 below shows the zig zag pattern that was created using the software, with dimensions in millimeters. The contact pads in the pattern consist of a square with side length 0.6 mm, and a square with side length 1.2 mm right next to it.

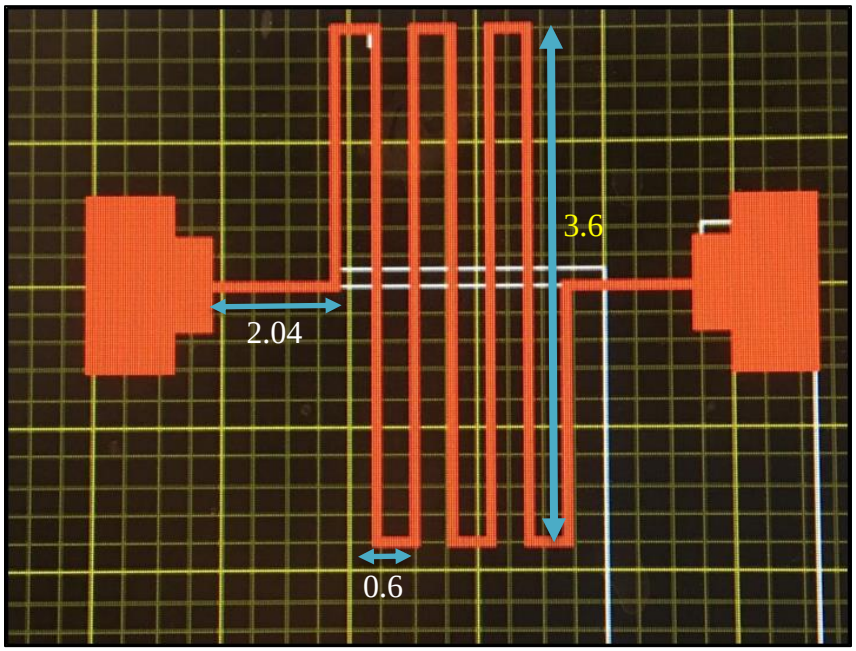

Figure 38. Zig zag print pattern

The zig zag pattern and the inkjet printing software was used to print the pattern. We set the delay time between drops to two seconds, and the print consisted of four layers or passes. Multiple attempts were needed in order to successfully print the zig zag pattern. One of the issues that we constantly ran into was that there would be gaps in the print that were only noticeable under a microscope. The small gaps would also occur at random points. Gaps in the print create

an open circuit, so it was important to figure out how to avoid gaps. In some of the prints, we noticed that some drops would form large puddles. This may indicate a problem with the time between drops or an issue with the PDMS surface. In particular, the PDMS surface can be filled with dust particles that can mix with the PEDOT ink drops. In addition, the jet head had a tendency to clog at times, so we had to monitor the print at all times and make sure that the printing system was still functioning. In order to fix the issues, we cleaned the PDMS substrate using DI water and used a duster to blow off any dust particles that were on the surface. We then printed the pattern, shown in Figure 39, successfully.

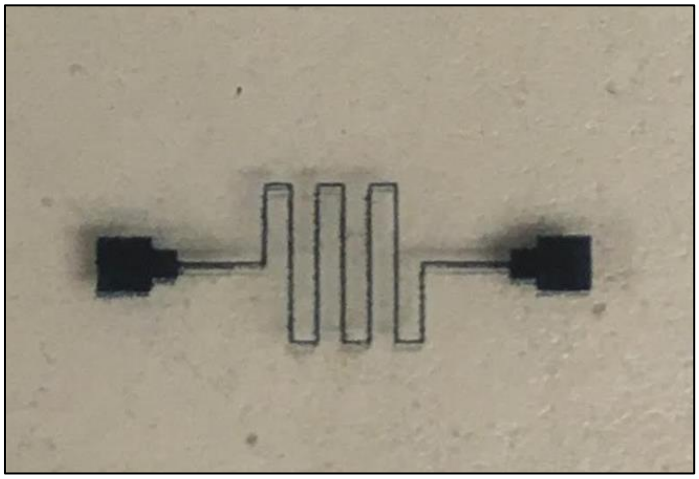

Figure 39. Printed zig zag pattern

The printed pattern was checked under a microscope in order to ensure that there were no gaps. Figure 40 shows an IC Capture image of the contact pads from the side.

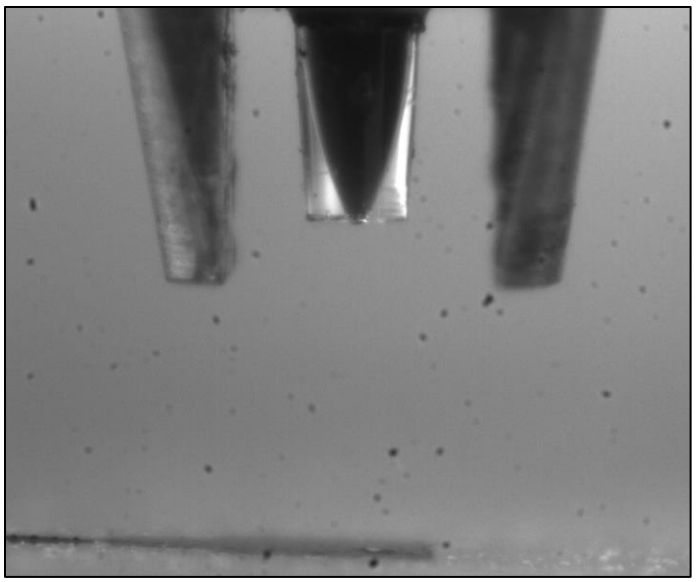

Figure 40. Contact pads

The printed pattern was used to fabricate the device. For fabrication, we used a number of different materials, such as copper tape, Kapton tape, and acetone. In order to create the device, we cut strips of copper tape and used acetone in order to remove the tape adhesive. This was done so that the adhesive does not heat up the copper tape and subsequently melt the substrate and the printed pattern. The adhesive was also removed so that it does not degrade the electrical connection between the printed device and the copper tape. Copper tape was used because it is fairly conductive. A wire cutter was used to cut strips of wires, and a wire stripper was used to remove the wire jackets at the ends of each wire. The wires were cut so that they had short leads. It is important that when we take resistance measurements, we reduce the effect of external sources. A longer wire tends to produce more resistance, so we want the wires and leads to be short. A soldering iron was used to join the wires and the copper tape strips. A syringe was used to put small amounts of Ag 150 (Harima Chemicals, Japan), a form of silver ink, on the contact pads. This was done so that any gaps in the contact pad are filled with conductive material. The copper

tape strips were then placed on top of the contact pads and placed so that the zig zag pattern was not covered. The contact pads allow current to go across the printed pattern and device.

To hold the copper tape in place, we used strips of Kapton tape. The strips of Kapton tape were placed so that they cover most of the copper tape strips. It was important to make sure that the Kapton tape was firmly attached to the copper tape and the glass slide. Figure 41 shows the fully created device from a top view. A digital multimeter was used to make sure that the device has a finite resistance.

Figure 41. Fully fabricated resistive device

A 3 by 3 array pattern was also printed. The array contains nine different devices or pixels. A successful 3 by 3 array can be used to produce a larger thermal image. Figure 42 shows the 3 by 3 array pattern that we came up with, and Figure 43 shows the printed array with copper tape attached to some contact pads. The dimensions in Figure 42 are in millimeters. The contact pads are made of squares with side length 0.84 mm.

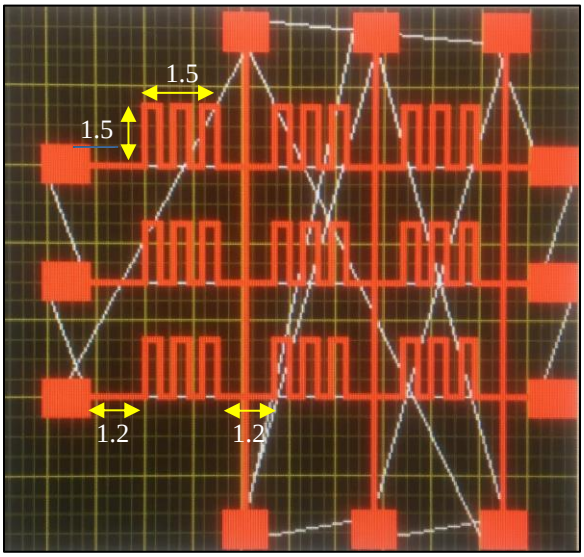

Figure 42. 3 by 3 array pattern

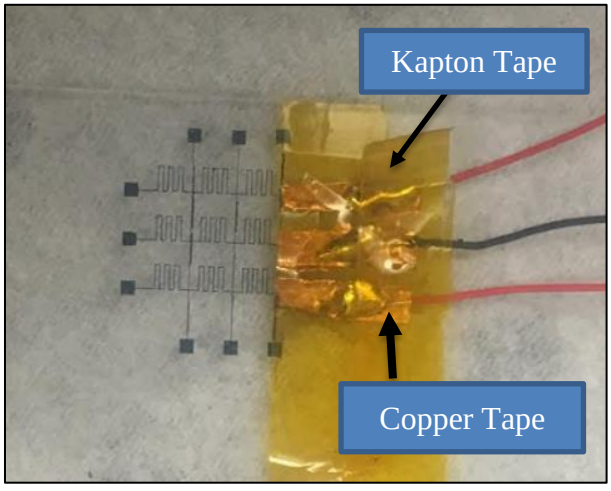

Figure 43. Printed 3 by 3 array pattern

Chapter 5. DEVICE TEST RESULTS

In order to assess the performance of the device, we measured the resistance as a function of the PDMS temperature. We also put different sources of heat above the sensing area to see how sensitive the device was at different temperatures. The sensitivity of the device was assessed by making the resistance changes that occurred once the heat source was placed above the sensing area. For the tests, we used a cold steel rod and a finger as our sources. The heat sources were placed at different distances above the sensing area so that we can see what the detection range of the device is. The results from the experiments that were done are summarized in this chapter.

5.1 TEST SET-UP

A digital hot plate was used to heat up the PDMS that the device was built on. The hot plate temperature could be set above room temperature. However, it was important to make sure that the temperature was not set too high because the PEDOT may melt at extreme temperatures. Therefore, the temperatures that we tested with the hot plate were between 30^{o}C and 50^{o}C. After setting the hot plate temperature, we used an infrared temperature gun in order to measure the temperature of the sensing area and PDMS. It was discovered that the reading on the infrared temperature gun did not necessarily match the hot plate temperature. Therefore, there were instances in which the hot plate temperature was adjusted so that the actual PDMS temperature would match the temperature that we desired. The top of the hot plate was covered with aluminum foil, and the device was placed flat with the sensing area facing up. Alligator clips were attached to the wires of the device. The resistance across the device was measured with a Hewlett Packard

34401A multimeter. We used a two-wire resistance measurement method for taking measurements. The initial measurement set-up is shown in Figure 44.

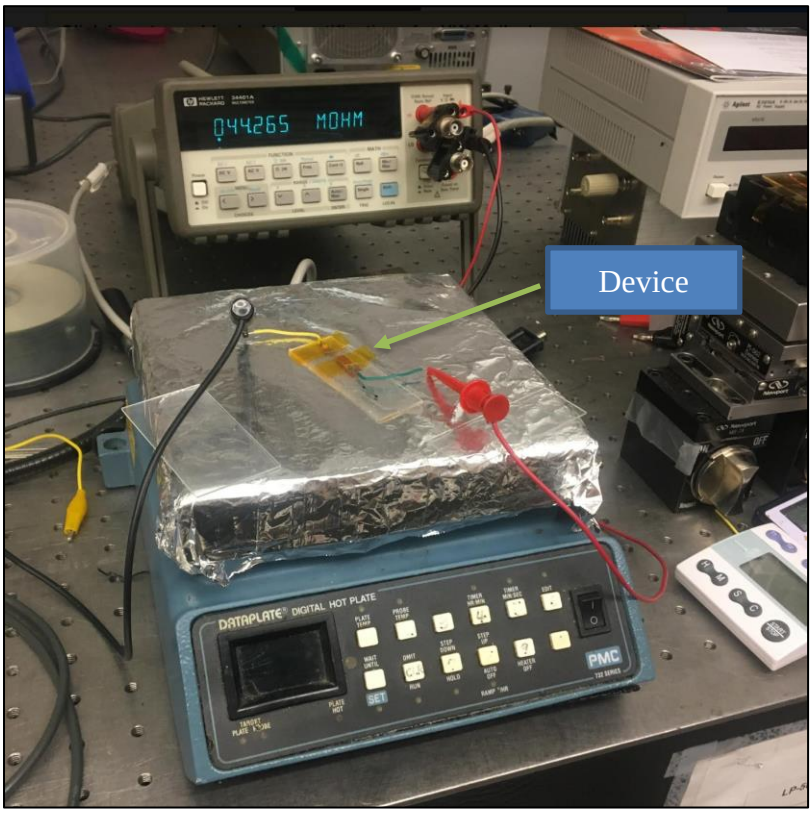

Figure 44. Initial resistance measurement set-up

5.2 Resistance vs Substrate Temperature

The PDMS substrate was heated to 30, 40, and 50 degrees Celsius. At each temperature, five sets of resistance measurements were initially taken with no heat source above the sensing area. We took five sets of measurements because there were some slight fluctuations in the resistance when taking measurements. The fluctuations may be a result of electrical noise in the lab where the experiments were done. We took multiple sets of resistance measurements so that we can see if the results are consistent. There were some slight differences between the resistance

measurement sets, but as a whole, the measurements were fairly similar. The measurements that were taken are shown in Table 4. The resistance values in the table are in Mega Ohms (MOhms).

Table 4. Resistance measurements at different PDMS temperatures

PDMS Temperature (ºC)	**R1**	**R2**	**R3**	**R4**	**R5**	**Average Resistance**
30	33.122	33.120	33.319	33.277	33.199	33.207
40	28.844	28.879	28.931	28.843	28.712	28.842
50	23.119	23.121	23.130	23.111	23.044	23.105

From the measurements, the average resistance change per temperature is (23.105-33.207) MOhms / (50-30)ºC = -0.5051 MOhms/ºC. The error in resistance was computed for each temperature. Figure 45 below shows the average resistance vs PDMS temperature with error bars. The error ranged from 0.016 to 0.04 MOhms, which means that the resistance was extremely consistent.

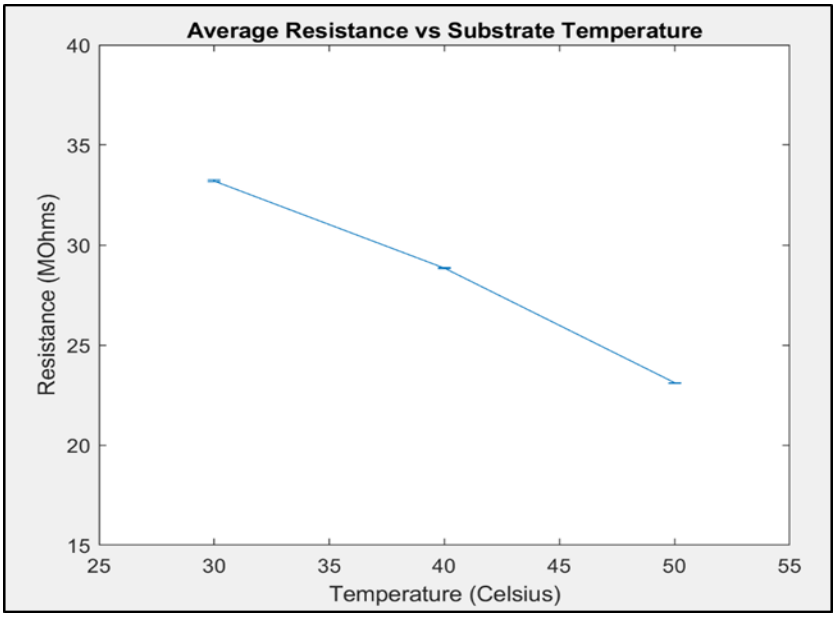

Figure 45. Average resistance vs PDMS temperature with error bars

An ANSYS simulation was also used to see what the resistance change per substrate or device temperature should theoretically be. The change in resistance per substrate temperature from the ANSYS simulation was -0.41621 MOhms/^{o}C, which is similar to the value obtained from the measurements from 30^{o}C to 50^{o}C. The slight difference between the measured data and the simulation is mainly due to the shelf life of the PEDOT. During the limited shelf life, certain properties, such as the electrical conductivity of the PEDOT, can change significantly.

5.3 Resistance Change vs Source Distance Above Room Temperature

To determine the sensitivity of the device, we placed different objects above the sensing area. Afterwards, the resistance was measured. For each case, we took five sets of measurements and computed the average resistance and resistance change. The resistance change is the difference between the resistance when there is an object above the sensing area and the resistance with no object or heat source. A set-up of the sensitivity test set-up is shown in Figure 46. We first placed a steel rod above the device. The steel rod was cooled to a temperature of 14.5^{o}C and placed horizontally above the device sensing area. A thermocouple was used to make sure that the steel rod was at the desired temperature. The steel rod is 10.1 cm long, with a diameter of 1.25 cm.

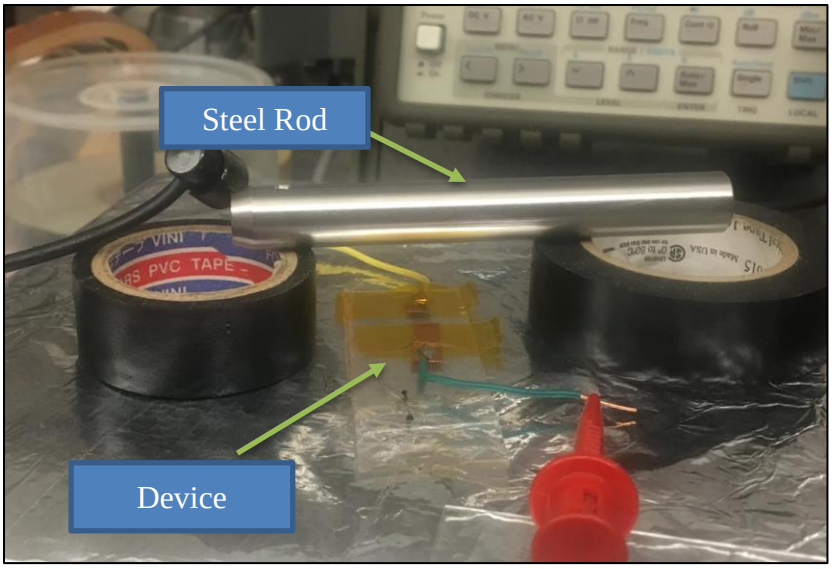

Figure 46. Sensitivity test set-up

The resistance measurements were taken with the rod placed at different distances above the sensing area and the substrate heated above room temperature. Table 5 shows the resistance data that was collected for the steel rod. The resistance and resistance change values are in Mega Ohms.

Table 5. Sensitivity test results with 14.5^{o}C steel rod above the sensing area

PDMS Temperature (^{o}C)	R1	R2	R3	R4	R5	Average Resistance	Average Resistance Change
Rod Distance: 4.75 mm							
30	30.578	30.633	30.662	30.707	30.746	30.665	-2.542
40	28.329	28.125	28.286	28.649	28.552	28.388	-0.454
50	23.226	23.357	23.373	23.449	23.518	23.385	0.280
Rod Distance: 7.75 mm							
30	32.826	32.975	33.110	33.114	33.343	33.074	-0.134
40	29.186	29.042	29.053	29.190	29.228	29.140	0.298
50	23.007	23.001	23.061	23.041	23.169	23.056	-0.049
Rod Distance: 16.75 mm							
30	32.253	32.243	32.007	32.035	32.083	32.124	-1.083
40	28.680	28.645	28.414	28.606	28.674	28.604	-0.238
50	23.000	22.955	22.926	22.872	22.884	22.927	-0.178
Rod Distance: 23.75 mm							
30	33.513	33.292	33.301	33.343	33.419	33.374	0.166
40	28.023	27.936	27.926	28.194	28.009	28.018	-0.824
50	23.155	22.992	22.962	23.014	23.042	23.033	-0.072

The error in the resistance change was computed for each case. Figure 47 shows the average resistance change as a function of the rod distance, with error bars. The resistance change error ranged from 0.02 to 0.119 MOhms.

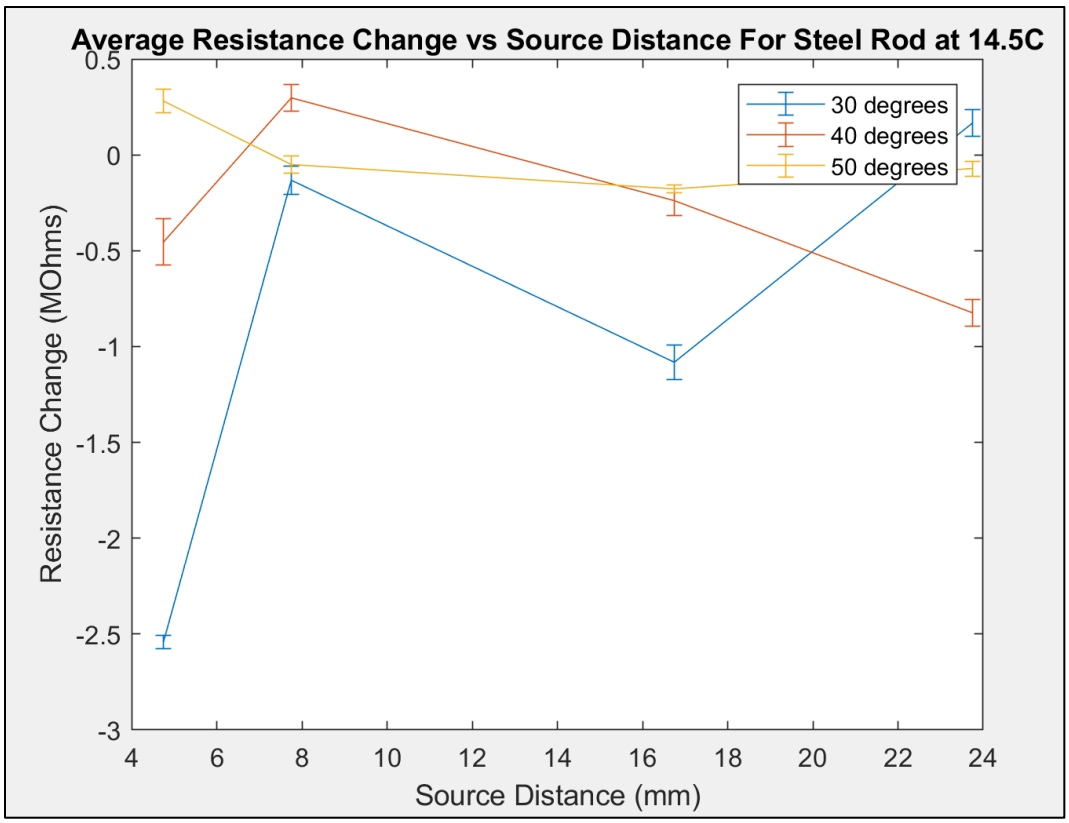

Figure 47. Average resistance change vs 14.5ºC steel rod distance with error bars

A Peltier heater was used to heat up the steel rod to 50.5ºC. The same tests were performed so that we can see how the device detects the same rod when the material temperature changes. The resistance and resistance changes for the 50.5ºC steel rod are listed in Table 6.

Table 6. Sensitivity test results with 50.5ºC steel rod above the sensing area

PDMS Temperature (ºC)	R1	R2	R3	R4	R5	Average Resistance	Average Resistance Change
Finger Distance: 4.75 mm							
30	32.325	32.277	32.241	32.187	32.154	32.237	-0.971
40	28.429	28.397	28.574	28.525	28.355	28.456	-0.386
50	23.119	22.946	22.880	22.888	22.920	22.951	-0.154
Finger Distance: 7.75 mm							
30	33.273	33.223	33.208	33.167	33.193	33.213	0.005
40	28.913	28.772	28.752	28.741	28.732	28.782	-0.060
50	23.151	23.182	23.105	23.085	23.103	23.125	0.020
Finger Distance: 16.75 mm							
30	33.211	33.199	33.266	33.387	33.037	33.220	0.013
40	28.681	28.747	28.788	28.761	28.739	28.743	-0.099
50	23.220	23.162	23.160	23.232	23.074	23.170	0.065
Finger Distance: 23.75 mm							
30	33.024	33.018	32.984	32.986	33.013	33.005	-0.202
40	29.127	29.054	29.089	29.105	29.078	29.091	0.249
50	23.135	23.159	23.213	23.089	23.069	23.133	0.028

The resistance change error was computed for all cases. Figure 48 shows the average resistance change vs the rod distance, with error bars. The resistance change error ranged from 0.017 to 0.062 MOhms.

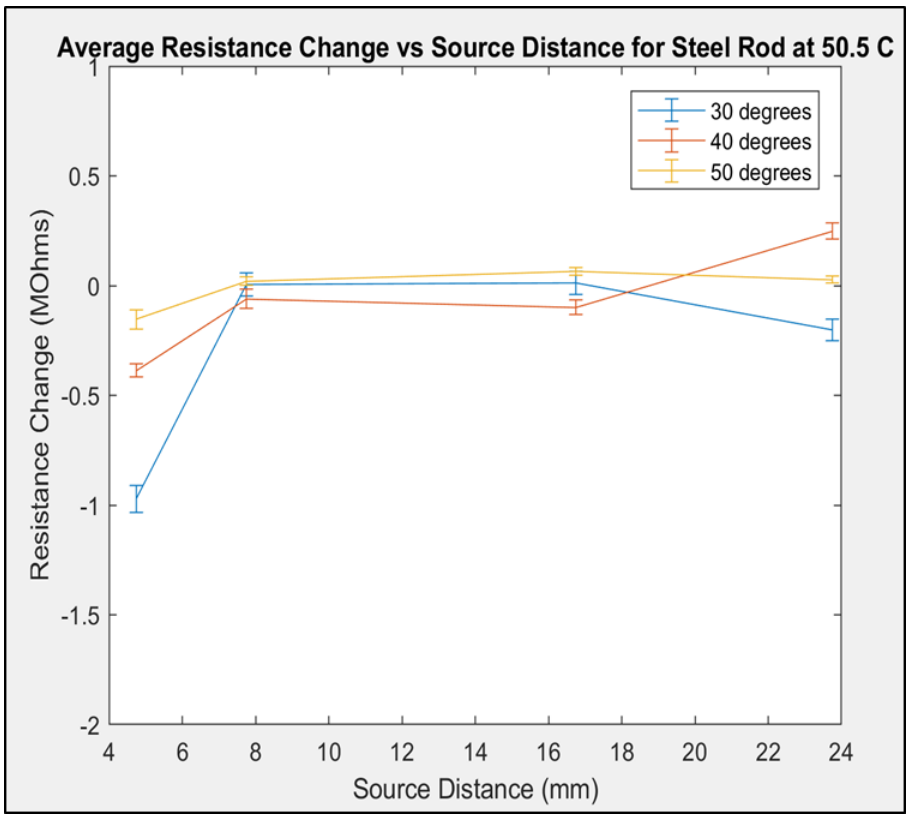

Figure 48. Average resistance change vs 50.5ºC steel rod with error bars

We also performed the same test with a finger above the device instead of a steel rod. This was done in order to see how the device detects different materials. The finger had a temperature of 35.9ºC. The resistance and resistance changes for the test with the finger are listed in Table 7.

Table 7. Sensitivity test results with finger above the sensing area

PDMS Temperature (ºC)	R1	R2	R3	R4	R5	Average Resistance	Average Resistance Change
Finger Distance: 4.75 mm							
30	42.144	42.670	42.485	41.773	42.111	42.237	9.029
40	34.408	34.585	33.465	34.107	33.975	34.108	5.266
50	27.050	26.727	27.672	27.111	26.447	27.001	3.896
Finger Distance: 7.75 mm							
30	36.321	37.987	37.458	36.560	37.301	37.125	3.918
40	30.965	30.094	30.020	29.790	29.661	30.106	1.264
50	24.385	24.381	25.518	24.522	24.514	24.664	1.559
Finger Distance: 16.75 mm							
30	33.693	33.956	33.800	33.689	33.540	33.736	0.528
40	28.900	28.727	28.729	28.839	28.627	28.764	-0.077
50	22.730	22.627	22.578	22.559	22.592	22.617	-0.488
Finger Distance: 23.75 mm							
30	33.389	33.301	33.802	33.191	33.310	33.399	0.191
40	28.545	28.520	28.256	28.405	28.242	28.394	-0.448
50	23.063	23.243	23.092	22.925	22.315	22.928	-0.177

The error in the resistance change was computed for each case, just like it was done with the steel rod. Figure 49 shows the average resistance change vs the finger distance, with error bars. The resistance change error ranged from 0.031 to 0.309 MOhms.

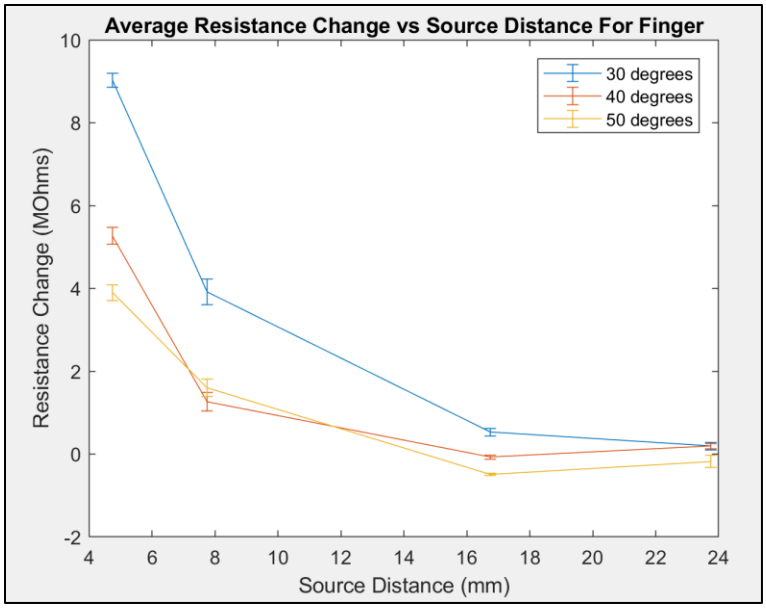

Figure 49. Average resistance change vs finger distance with error bars

5.4 Resistance Change vs Source Distance Below Room Temperature

The sensitivity of the device was also evaluated after the device was cooled. In order to cool the device, a freeze pack that had been stored in a freezer was placed underneath the device. The hot plate was turned off. Afterwards, the resistance of the device was measured at five different instances with no object above the source. Figures 50 and 51 show the initial measurement set-up.

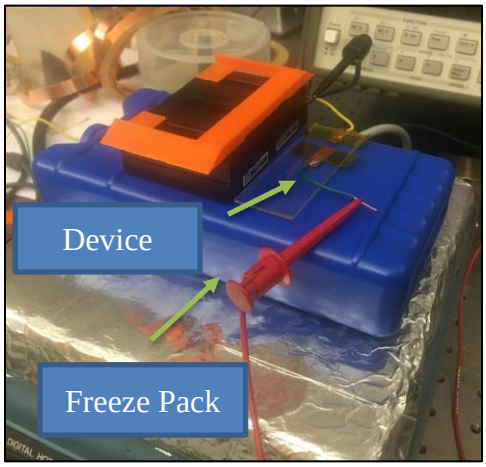

Figure 50. Measurement set-up with freeze pack underneath

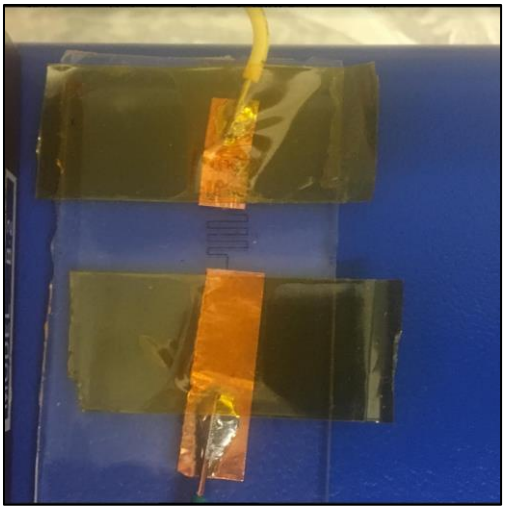

Figure 51. Top view of the measurement set-up with freeze pack underneath

The resistance measurements are shown in Table 8, with the measurements in units of Mega Ohms.

Table 8. Resistance measurements with PDMS around freezing temperature

R1	**R2**	**R3**	**R4**	**R5**	**Average Resistance**
74.249	74.226	73.945	73.870	73.502	73.958

We performed the same sensitivity tests that were done when the PDMS was heated above room temperature. The 14.5^{o}C steel rod and finger were placed at the same distances as the previous tests. The resistance and resistance change values that were obtained from the rod and finger are listed in Table 9.

Table 9. Sensitivity test results with PDMS around freezing temperature

Object	R1	R2	R3	R4	R5	Average Resistance	Average Resistance Change
Object Distance: 4.75 mm							
Steel Rod	71.167	70.654	69.807	69.431	68.977	70.007	-3.951
Finger	19.578	20.281	20.182	19.634	20.260	19.987	-53.971
Object Distance: 7.75 mm							
Steel Rod	73.632	73.430	72.983	72.794	72.931	73.154	-0.804
Finger	36.324	36.257	36.571	34.491	39.278	36.584	-37.374
Object Distance: 16.75 mm							
Steel Rod	73.830	73.905	73.866	73.849	73.714	73.833	-0.126
Finger	75.803	73.655	72.135	71.656	71.386	72.927	-1.032
Object Distance: 23.75 mm							
Steel Rod	74.062	74.239	74.310	74.188	73.821	74.124	0.166
Finger	74.553	73.625	73.235	73.017	72.130	73.312	-0.646

For both the steel rod and finger tests, the error in resistance change between the five sets of measurements was computed. The error ranged from 0.097 to 0.274 MOhms for the steel rod and 0.238 to 0.854 MOhms for the finger. Figure 52 shows the average resistance change as a function of the source distance with error bars for both objects.

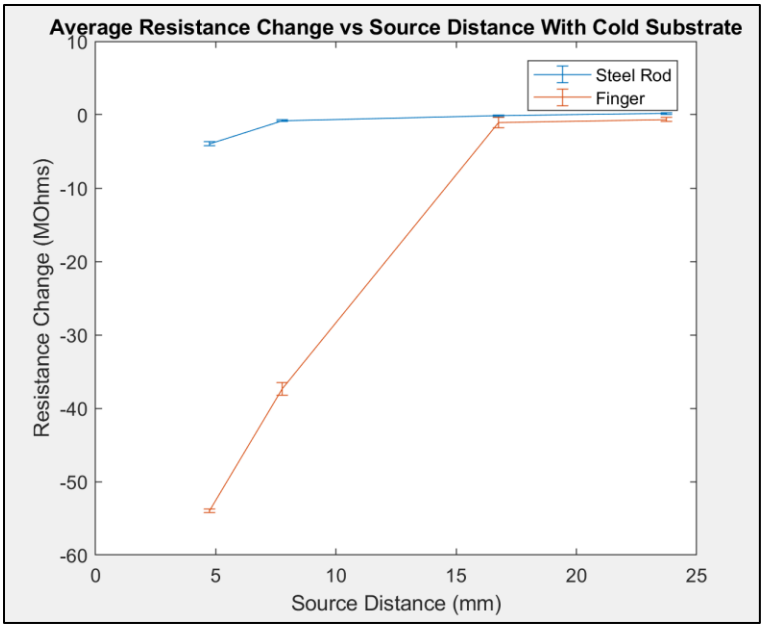

Figure 52. Average resistance change vs source distance with PDMS around freezing temperatures

5.5 Discussion

As a whole, the results from the device are promising. The device displays a fairly large resistance change in most cases. The device appears to detect the finger much better than the steel rod, as indicated by the larger resistance changes that occur when the finger is placed above the device. This may be due to certain material properties of the steel rod, such as its thermal conductivity. The finger may be absorbing some of the heat in the system when it is placed near the device. The device seems to consistently detect the finger as long as it is within 15-17 mm of the sensing area. On the other hand, the steel rod seems detectable at larger distances, even though the resistance change is much smaller.

The substrate temperature also impacts the amount of resistance change that occurs. It is clear that the resistance change decreases as the substrate temperature increases when the finger is placed above the sensing area. However, the resistance change is much more unpredictable when

the steel rod is used. When the PDMS temperature was at 30^{o}C and 40^{o}C, the resistance change decreased and increased at certain distances with the rod. At 40^{o}C, the resistance change goes from positive to negative when the rod is at a distance of about 6 mm. This transition point may occur due to the way in which the rod radiates energy, or the electrical behavior of the PEDOT. At 50^{o}C, the resistance change constantly decreases as the distance between the rod and the device increases. This is the behavior that we should expect. The resistance change is also positive for the most part when the PDMS temperature is at 50^{o}C. In addition, when the PDMS is close to freezing temperature, the resistance change is significantly larger for both the steel rod and finger. The resistance change consistently decreases as the object distance decreases. Based on the results, the device has the capability to detect different objects. The resistance change that occurs when the device detects a human finger is much more consistent that the change that occurs from a steel rod. For this particular device, a PDMS temperature around 50^{o}C or freezing temperature seems ideal because at those temperatures, the resistance change decreases in a similar manner for both the steel rod and the finger. When the PDMS substrate is somewhat close to the surrounding temperature, the resistance change is somewhat random when the device detects an object other than human skin. The surrounding temperature was around 21^{o}C. The device may be less susceptible to noise as the difference between the substrate temperature and room temperature increases. Overall, the device displays an excellent ability to detect objects, considering how small and thin the device is. This device has several advantages over traditional devices, such as higher sensitivity, simpler and smaller design, and cost.

5.6 3 BY 3 ARRAY AND ISSUES

A thermal image can be obtained from the 3 by 3 array by measuring the resistance and resistance change across all nine pixels. Due to the array design, the mesh detection scheme may be needed to determine the resistance across certain pixels. The resistance across certain pixels cannot be measured directly through probes. For these pixels, the resistance is calculated based on the resistance across other pixels that can be measured directly. Before taking any measurements on the array, a simulation was used to see an example of a thermal image that may be obtained from the 3 by 3 array if an object is placed above certain pixels in the array. Figure 53 shows a thermal image based on an ANSYS simulation.

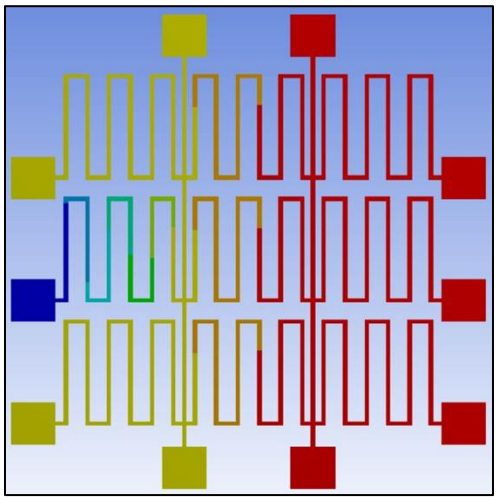

Figure 53. Thermal image from 3 by 3 array – obtained from ANSYS simulation

Afterwards, we attempted to take measurements on the 3 by 3 array. Initially, we tried placing probes gently on the printed contact pads to get resistance measurements. However, the resistance readings fluctuated quite heavily, which makes the data unusable. We then tried to place copper tape and soldered wires on the pads so that we can hook up the soldered wires to the

multimeter. This did not fix the resistance readings. Instead, we got an open circuit. For the array, we may need to increase the distance between the pads so that we can get consistent resistance readings. An ANSYS simulation was used to run a simulation on the 3 by 3 array and see what the resistance across one of the devices in the array may be. Figure 54 shows a simulation that was done on the array.

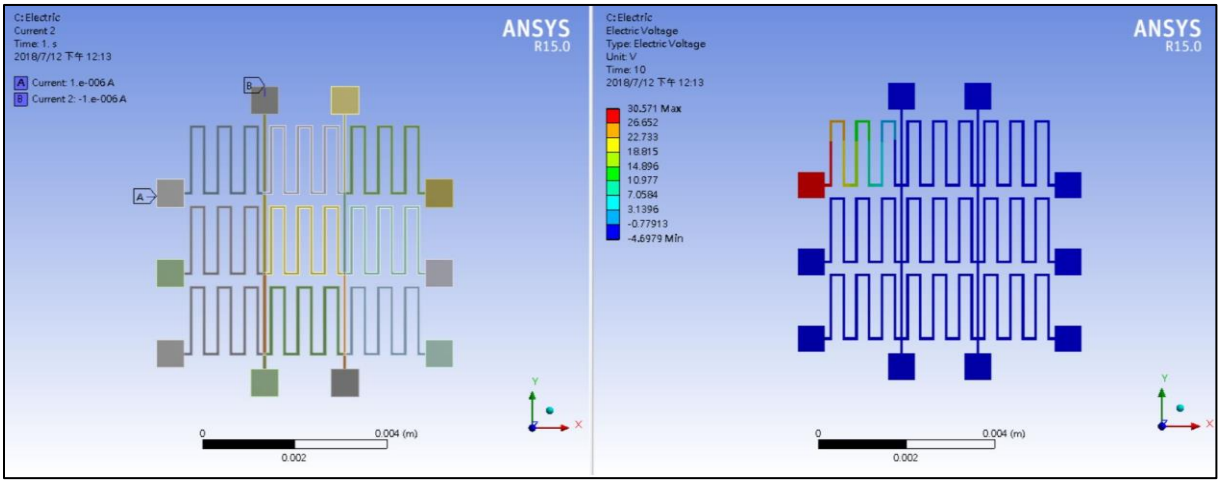

Figure 54. 3 by 3 array sample simulation

Chapter 6. CONCLUSION AND FUTURE WORKS

An in-house inkjet printing system was used to successfully fabricate a thermal resistive device that can be used in thermal imaging applications. The resistive thermal imaging device is simpler and smaller in design compared to traditional thermal imaging devices. In addition, the device that was created is relatively cheap and quick to fabricate. The in-house inkjet printing system was controlled through a written LabVIEW program that can be used to customize 2D and 3D printing. The imaging device was primarily made of PEDOT, which is a polymer with excellent electrical conductivity. Printing was done on PDMS substrates. The device was then analyzed through a number of tests in order to determine how the device functions under certain conditions. Additional filters or amplifiers were not needed to obtain data from the tests. The tests show that the device is highly sensitive regardless of the object that it senses. As the substrate temperature increases, the resistance change in the device decreases. The amount of resistance change decreases as the distance between the object and device increases. However, the decrease in resistance change is much more consistent for all objects when the PDMS temperature is much higher or lower than the ambient temperature. Electrical noise may impact the performance of the device if the substrate temperature is similar to the ambient temperature.

Future work can be done in order to see how the resistance change in the device is impacted by the material properties of the objects that the device detects. It is possible that the geometry of an object affects the way the device detects the object. Furthermore, devices can be printed on other substrates. Different polymers can be used for printing the device. In terms of design, circular patterns can also be looked at for the sensing area of the devices. The inkjet printing system and software that was used for this research had limitations when it came to processing circular or

curved patterns. Therefore, we used a zig zag pattern that consists of straight lines. It would be useful to see how the sensitivity of the device changes if a circular pattern is used. The 3 by 3 device array could also be re-printed and fabricated in the future in order to determine whether a 2D temperature profile can be seen when an object is detected by a device in the array. The array may also be used to see how a thermal image changes in multiple directions when the devices in the array sense different objects. Different array circuits, such as the ones in Figure 55, and larger scale arrays with higher pixel resolutions can also be explored. If array patterns can be successfully printed, then there is a possibility that the printed arrays can be converted into a soft, flexible wearable sensor that can be used in real-life applications.

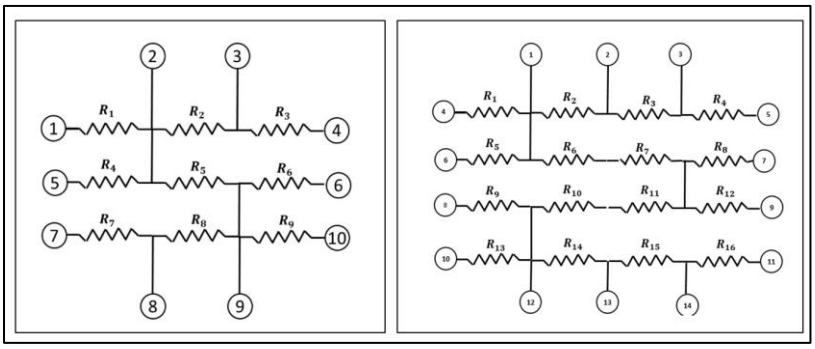

Figure 55. Array circuits. The resistors in the circuits represent pixels, and the circled numbers represent contact pads.

BIBLIOGRAPHY

[1] Bhavar, V., Kattire, P, Patil, V., Khot, S., Gujar, K., Singh, R., 2014, "A Review on Powder Bed Fusion Technology of Metal Additive Manufacturing," *4th International Conference And Exhibition On Additive Manufacturing Technologies*

[2] Hoeng, F., Bras, J., Gicquel, E., Krosnicki, G., Denneulin, A., 2017, "Inkjet printing of nanocellulose–silver ink onto nanocellulose coated cardboard," RSC Advances, **7**(25), pp. 15372-15381

[3] Seuser, A., Kurnik, K., Mahlein, A., 2018, "Infrared Thermography as a Non-Invasive Tool to Explore Differences in the Musculoskeletal System of Children with Hemophilia Compared to an Age-Matched Healthy Group," Sensors, **18**(2), pp. 1-10

[4] Niklaus, F., Vieider, C., Jackobsen, H., 2008, "MEMS-Based Uncooled Infrared Bolometer Arrays – A Review," *Proceedings of SPIE*, **6836**

[5] Hyseni, G., Caka, N., Hyseni, K., 2010, "Infrared Thermal Detectors Parameters: Semiconductor Bolometers Versus Pyroelectrics," WSEAS Transactions on Circuits and Systems, **9**(4), pp. 238-247

[6] Hsiao, C. and Liu, S., 2014, "Multi-Frequency Band Pyroelectric Sensors," Sensors, **14**(12), pp. 22180-22198

[7] Sassi, U., Parret, R., Nanot, S., Bruna, M., Borinin, S., De Fazio, D., Zhao, Z. Lidorikis, E., Koppens, F., Ferrari, A., Colli, A., 2017, "Graphene-based mid-infrared room-temperature pyroelectric bolometers with ultrahigh temperature coefficient of resistance," Nature Communications, **8,** pp.1-10

[8] Li, J., Taylor, A., Papakonstantinou, I., Zhang. E., Beard, P., 2014, "Highly sensitive optical microresonator sensors for photoacoustic imaging," *Proceedings of SPIE*, **8943**

[9] Strasser, F., Melnik, E., Muellner, P., Jiménez-Meneses, P., Nechvile, M., Koppitsch, G., Lieberzeit, P., Laemmerhofer, M., Heer, R., Hainberger, R., 2017, "Preparation of Mach-Zehnder interferometric photonic biosensors by inkjet printing technology," *Proceedings of SPIE*, **10231**

[10] Ruecha, N., Chailapakul, O., Suzuki, K., Citterio, D., 2017, "Fully Inkjet-Printed Paper-Based Potentiometric Ion-Sensing Devices," Analytical Chemistry, **89**(19), pp. 10608-10616

[11] Sielmann, C., Busch, J., Stoeber, B., Walus, K., 2013, "Inkjet Printed All-Polymer Flexural Plate Wave Sensors," IEEE Sensors Journal, **13**(10), pp. 4005-4013

[12] Kehrt, M., Monte, C., Beyer, J., Hollandt, J., 2015, "A highly linear superconducting bolometer for quantitative THz Fourier transform spectroscopy," Optics Express, **23**(9), pp. 11170-11182

[13] Cherednichenko, S., Hammar, A., Bevilacqua, S., Drakinskiy, V., Stake, J., Kalabukhov, A., 2011, "A Room Temperature Bolometer for Terahertz Coherent and Incoherent Detection," IEEE Transactions on Terahertz Science and Technology, **1**(2), pp. 395-402

[14] Schossig, M., Norkus, V., Gerlach, G., 2010, "Infrared Responsivity of Pyroelectric Detectors With Nanostructured NiCr Thin-Film Absorber," IEEE Sensors Journal, **10**(10), pp. 1564-1565

[15] Socher, E., Sinai, Y., Nemirovsky, Y., 2003, "A Low-Cost CMOS Compatible Serpentine-Structured Polysilicon-Based Microbolometer Array," *12th International Conference on Solid-State Sensors, Actuators, and Microsystems*, **1**, pp. 320-323

[16] Modarres-Zadeh, M. and Abdolvand, R., 2014, "High-responsivity thermoelectric infrared detectors with stand-alone sub-micrometer polysilicon wires," Journal of Micromechanics and Microengineering, **24**(12), pp. 1-9

[17] Mata, A., Fleischmann, A., Roy, S., 2005, "Characterization of Polydimethylsiloxane (PDMS) Properties for Biomedical Micro/Nanosystems," Biomedical Microdevices, **7**(4), pp. 281-293